



# Compact high order finite volume method on unstructured grids IV: Explicit multi-step reconstruction schemes on compact stencil



Yu-Si Zhang<sup>a</sup>, Yu-Xin Ren<sup>a,\*</sup>, Qian Wang<sup>b</sup>

<sup>a</sup> Department of Engineering Mechanics, Tsinghua University, Beijing 100084, China

<sup>b</sup> Mathematics Section, Ecole Polytechnique Fédérale de Lausanne, CH-1015 Lausanne, Switzerland

## ARTICLE INFO

### Article history:

Received 9 November 2018

Received in revised form 21 June 2019

Accepted 22 June 2019

Available online 28 June 2019

### Keywords:

High order schemes

Finite volume methods

Unstructured grids

Multi-step reconstruction

## ABSTRACT

In the present paper, a multi-step reconstruction procedure is proposed for high order finite volume schemes on unstructured grids using compact stencil. The procedure is a recursive algorithm that can eventually provide sufficient relations for high order reconstruction in a multi-step procedure. Two key elements of this procedure are the partial inversion technique and the continuation technique. The partial inversion can be used not only to obtain lower order reconstruction based on existing reconstruction relations, but also to regularize the existing reconstruction relations to provide new relations for higher order reconstructions. The continuation technique is to extend the regularized relations on the face-neighboring cells to current cell as additional reconstruction relations. This multi-step procedure is operationally compact since in each step only the relations defined on a compact stencil are used. In the present paper, the third and fourth order finite volume schemes based on two-step quadratic and three-step cubic reconstructions are studied.

© 2019 Elsevier Inc. All rights reserved.

## 1. Introduction

High order methods have shown great capability in the simulation of flows with multi-scale structures [1]. To handle complicated geometries, various high order numerical methods on the unstructured grids have been developed such as the finite volume (FV) methods [2–9,56,57], discontinuous Galerkin (DG) methods [10–14], spectral volume (SV)/spectral difference (SD) methods [15–21], P<sub>N</sub>P<sub>M</sub> procedure [22–24] and the hybrid FV/DG methods [25,26].

Historically, the high order FV methods on the unstructured grids were among the numerical schemes that received earliest attention since they are simpler to construct and implement. The key point of FV schemes is to reconstruct high order representation of the solutions in each cell or control volume. The k-exact FV method was developed by Barth and Frederickson [2]. ENO and WENO schemes were then developed [6,27–36]. The high order FV schemes usually require a large number of cells in the stencil of the reconstruction procedure. The large stencil problem is a serious drawback of the traditional FV schemes. It may result in algorithmic complexity [37] in searching and identification of the stencil, large memory requirement to store the stencil and the reconstruction coefficients [25], difficulty in boundary treatment,

\* Corresponding author.

E-mail address: ryx@tsinghua.edu.cn (Y.-X. Ren).

and impairment of the scalability of the code in parallel computation [51]. Therefore, the large stencil may pose a major obstacle for the application of the high order FV schemes in very large scale engineering simulations.

To overcome this problem, Wang and Ren developed the compact least squares reconstruction (CLSR) scheme [38,39] on compact stencil. This method is constructed by requiring the variable and its derivatives on the control volume of interest to conserve their averages on the face-neighboring cells. To ensure the non-singularity of the reconstruction procedure, the variational reconstruction (VR) procedure for the high order FV schemes on the unstructured grids was recently proposed [40]. This method can be also applied on a compact stencil and more importantly, can be proved to be non-singular on general shaped unstructured grids. Both CLSR and VR are implicit, and a large system of linear equations should be solved. To design an efficient solution procedure, the CLSR and VR are computed using a certain iterative solution procedure. When solving unsteady flows, they should be coupled with implicit dual time stepping procedure so that only one iteration is performed in each pseudo time step. Using this approach, the FV schemes based on CLSR and VR can be as efficient as those based on the k-exact reconstruction when the implicit time stepping schemes are used. However, when using the explicit time stepping schemes, these methods become less efficient because of the implicit nature of these schemes. Therefore, it is desirable to develop an explicit reconstruction algorithm on a compact stencil which can be readily applied in both explicit and implicit time marching schemes.

We notice some approaches with above-mentioned property have been proposed. For example, Yang et al. [41] used the Gauss-Green theorem successively to obtain high order distribution of the solution in a control volume. However, it is not able to prove if this approach has the property of k-exactness. Haider et al. [42] developed the *Coupled Least Squares* reconstruction by approximating derivatives from higher order to lower order. However, on the unstructured grids, this approach is depended on some claims that are not easy to prove and is very complicated. Chiravalle et al. [52] developed a two-step reconstruction, which is quite convenient to obtain 3rd order accuracy schemes. The main drawbacks of this method is that the accuracy is restricted to 3rd order.

In the present paper, the FV scheme based on a multi-step reconstruction (MSR) procedure is proposed on 1D mesh and 2D triangular mesh. The MSR is a recursive algorithm which can eventually provide sufficient relations for high order reconstruction in a multi-step procedure. Two key elements of this procedure are the partial inversion technique (PIT) and the continuation technique (CT). The PIT can be used not only to obtain lower order reconstruction based on existing reconstruction relations, but also to regularize the existing reconstruction relations to provide new relations for higher order reconstructions. The CT is to extend the regularized relations on the face-neighboring cells to current cell as additional reconstruction relations. In the implementation of MSR, one does not need to search and store the possible large stencil encountered in the high order FV schemes. Instead, during the implementation of MSR, the cells involved in the reconstruction will increase accordingly. Furthermore, this procedure is operationally compact in the sense that in every step of this multi-step procedure, only the information of current and face-neighboring cells is used. As being discussed in [40], this property is sufficient to ease the data transfer between different sub-domains in the parallel computing based on the domain decomposition approach and is also beneficial to reduce the cache missing encountered by traditional high order FV schemes using a very large stencil. The computational cost is only slightly larger than the traditional k-exact reconstruction using large stencil.

This paper is organized as follows. Section 2 and Section 3 detail the MSR algorithms on 1D and 2D unstructured meshes respectively. In Section 4, numerical results of 1D tests and 2D tests are presented. Finally, conclusions are given in Section 5.

## 2. High order compact multi-step reconstructions for FV schemes: the 1D case

### 2.1. Notations and the basic ideas of the multi-step reconstruction

In this section, the 1D MSR is introduced and the spectral property for corresponding high order FV schemes is analyzed. To facilitate the derivation, some notations are introduced first. In 1D FV methods, the physical domain  $\Omega$  is decomposed into  $N$  non-overlapping control volumes (cells).  $\Omega_i \equiv [x_{i-1/2}, x_{i+1/2}]$  is the  $i$ th cell.  $h_i = x_{i+1/2} - x_{i-1/2}$  is the length of  $\Omega_i$  and  $x_i = (x_{i-1/2} + x_{i+1/2})/2$  is the center of  $\Omega_i$ . We denote the cell average of variable  $u$  on  $\Omega_i$  as

$$\bar{u}_i = \frac{1}{h_i} \int_{\Omega_i} u(x) dx.$$

The reconstruction problem is to determine the piece-wise degree  $p$  polynomials that approximate  $u(x)$  to  $(p+1)$ th order of accuracy when the cell averages on all control volumes are specified. Specifically, on each cell  $\Omega_i$ , we need to calculate the unknown coefficients  $C_i^{(l)}$  of the following reconstruction polynomial

$$u_i(x) = C_i^0 + \sum_{l=1}^p C_i^{(l)} \psi_{l,i}(x), \quad (1)$$

where  $p$  is the degree of the polynomial, and  $\psi_{l,i}(x)$  is the Taylor basis defined by

$$\psi_{l,i}(x) = \frac{(x - x_i)^l}{(h_i)^l}.$$

Comparing with the Taylor expansion of  $u_i(x)$  about  $x_i$ , it is evident that

$$C_i^{(l)} = \left. \frac{\partial^l u}{\partial x^l} \right|_i \cdot \frac{h_i^l}{l!}. \quad (2)$$

There are many possible approaches to carry out the reconstruction procedure [2,6,27–36]. One common practice is to define a stencil consisting of  $q = m + n + 1$  control volumes

$$S_i = \{\Omega_{i-m}, \dots, \Omega_i, \dots, \Omega_{i+n}\},$$

and requires the following *reconstruction conditions* are satisfied exactly or in the sense of least squares,

$$\langle u_i(x) \rangle^j = \bar{u}_j, \quad j = i - m, \dots, i + n \quad (3)$$

where  $\Omega_j \in S_i$ , and

$$\langle u_i(x) \rangle^j = \frac{\int_{\Omega_j} u_i(x) dx}{h_j}.$$

To make the notations more clear, we use  $\bar{u}_j$  to denote the known cell average of the dependent variable on cell  $\Omega_j$  which is usually the solution of the FV schemes, and use  $\langle \bullet \rangle^j$  to denote the cell average of a reconstruction polynomial or one of its basis functions on cell  $\Omega_j$ . Eq. (3) leads to a system of linear equations

$$C_i^{(0)} + \sum_{l=1}^p C_i^{(l)} \langle \psi_{l,i}(x) \rangle^j = \bar{u}_j, \quad j = i - m, \dots, i + n. \quad (4)$$

If we choose  $q = p + 1$ ,  $C_i^{(l)}$  ( $l = 0, 1, \dots, p$ ) can be computed by solving Eq. (4), which is the case of WENO schemes [6,27–36]. When  $q > p + 1$  is chosen,  $C_i^{(l)}$  ( $l = 0, 1, \dots, p$ ) will be determined by solving the corresponding least squares problem as in the k-exact reconstructions [2]. In both cases, it is required that the conservation of cell average on  $\Omega_i$  is satisfied exactly, which lead to

$$C_i^{(0)} + \sum_{l=1}^p C_i^{(l)} \langle \psi_{l,i}(x) \rangle^i = \bar{u}_i. \quad (5)$$

To achieve this, Eq. (1) is modified into the following form by subtracting Eq. (5)

$$u_i(x) = \bar{u}_i + \sum_{l=1}^p C_i^{(l)} \phi_{l,i}(x) \quad (6)$$

where

$$\phi_{l,i}(x) = \psi_{l,i}(x) - \langle \psi_{l,i}(x) \rangle^i \quad (7)$$

is called the zero-mean basis [6,36]. This form of reconstruction polynomial guarantees that Eq. (5) is satisfied automatically. Using Eq. (6), the reconstruction conditions in Eq. (3) become

$$\sum_{l=1}^p C_i^{(l)} \langle \phi_{l,i}(x) \rangle^j = \bar{u}_j - \bar{u}_i, \quad j = i - m, \dots, i + n, \quad j \neq i. \quad (8)$$

Generally speaking, the degree  $p$  polynomial reconstruction will result in a  $(p + 1)$ th order accurate finite volume scheme. In what follows, the terms ‘degree  $p$  polynomial reconstruction’ and ‘ $(p + 1)$ th order accurate reconstruction’ are used interchangeably.

According to this introduction of the traditional polynomial reconstruction, it is evident that the number of cells in the reconstruction stencil should be equal to or greater than the number of unknown coefficients in the reconstruction polynomial. For the reconstructions with higher order of accuracy, this will lead to a large stencil. For 2D and 3D reconstructions, the stencils will be even larger. As being stated in Section 1, the large stencil problem may pose a major obstacle for the application of the high order FV schemes in very large scale engineering simulations.

In the present paper, a novel MSR algorithm is proposed to solve the large stencil problem. In this procedure, the high order accurate reconstruction is implemented in several steps. In each step, the algorithm is operationally compact in the

sense that only the information of current and face-neighboring cells is used [40]. To be specific, in 1D case, all operations in the algorithm should be based on the information defined on the compact stencil

$$S_i = \{\Omega_{i-1}, \Omega_i, \Omega_{i+1}\}. \quad (9)$$

To better illustrate the basic idea behind MSR, we use the 1D cubic reconstruction on uniform grid ( $h_i \equiv h$ ) as an example. In this case, Eqs. (6), (7) become

$$u_i(x) = \bar{u}_i + \sum_{l=1}^3 C_i^{(l)} \phi_{l,i}(x) \quad (10)$$

with

$$\phi_{1,i} = (x - x_i)/h, \quad \phi_{2,i} = (x - x_i)^2/h^2 - \frac{1}{12} \quad \text{and} \quad \phi_{3,i} = (x - x_i)^3/h^3$$

where  $h$  is the mesh size. The reconstruction conditions of Eq. (8) corresponding to the compact stencil of Eq. (9) consist of two equations that are

$$\begin{aligned} -C_i^{(1)} + C_i^{(2)} - \frac{5}{4}C_i^{(3)} &= \bar{u}_{i-1} - \bar{u}_i \\ C_i^{(1)} + C_i^{(2)} + \frac{5}{4}C_i^{(3)} &= \bar{u}_{i+1} - \bar{u}_i \end{aligned} \quad (11)$$

These two relations are not sufficient to compute the three unknowns in Eq. (10). To be able to compute the cubic reconstruction on the compact stencil, the first key idea of MSR is to seek the least squares solution of Eq. (11) only for the coefficients of the lower degree polynomial but all unknown coefficients are retained in this solution. In the first step of MSR, we only solve  $C_i^{(1)}$  using the least squares. The  $C_i^{(2)}$  and  $C_i^{(3)}$  terms are retained and moved to the right-hand-side. Therefore, we have

$$\begin{aligned} (a): -C_i^{(1)} &= \bar{u}_{i-1} - \bar{u}_i - C_i^{(2)} + \frac{5}{4}C_i^{(3)} \\ (b): C_i^{(1)} &= \bar{u}_{i+1} - \bar{u}_i - C_i^{(2)} - \frac{5}{4}C_i^{(3)} \end{aligned} \quad (12)$$

Eq. (12) is an overdetermined system to compute  $C_i^{(1)}$ . Eq. (12) is solved for  $C_i^{(1)}$  using the method of least squares, and the solution is identical to perform  $((b)-(a))/2$  where (a) and (b) are sub-equations of Eq. (12), i.e.

$$C_i^{(1)} = \frac{1}{2}(\bar{u}_{i+1} - \bar{u}_{i-1}) - \frac{5}{4}C_i^{(3)}. \quad (13)$$

This procedure is called the partial inversion technique in the (PIT) next sub-section since  $C_i^{(2)}$  and  $C_i^{(3)}$  are left unsolved. According to Eq. (2),  $C_i^{(3)} = O(h^3)$ . If the  $C_i^{(3)}$  term in Eq. (13) is neglected, one obtains

$$C_i^{(1)} = \frac{1}{2}(\bar{u}_{i+1} - \bar{u}_{i-1}) \quad (14)$$

which is exactly the linear k-exact reconstruction on a compact stencil. Eq. (14) is however not useful in performing higher order accurate reconstruction. The second key idea of the present paper is to retain the unknowns  $C_i^{(2)}$  and  $C_i^{(3)}$  in Eq. (13) and use Eq. (13) as the derived reconstruction relations for higher order accurate reconstruction, which is called the regularized reconstruction relation in the next sub-section. To keep the operation compact, it is denoted that

$$C_i^{(1)}|_{\text{step 1}} = \frac{1}{2}(\bar{u}_{i+1} - \bar{u}_{i-1}),$$

which is computed and stored. As the result, Eq. (13) can be written as

$$C_i^{(1)} = C_i^{(1)}|_{\text{step 1}} - \frac{5}{4}C_i^{(3)}. \quad (15)$$

The first step of the MSR procedure is to calculate (15) for all control volumes.

In the second step of the MSR, we use Eq. (15) obtained on cells belonging to the compact stencil of Eq. (9) as the new reconstruction relations, that are detailed as

$$\begin{cases} C_i^{(1)} = C_i^{(1)}|_{step\ 1} - \frac{5}{4}C_i^{(3)} \\ C_{i-1}^{(1)} = C_{i-1}^{(1)}|_{step\ 1} - \frac{5}{4}C_{i-1}^{(3)} \\ C_{i+1}^{(1)} = C_{i+1}^{(1)}|_{step\ 1} - \frac{5}{4}C_{i+1}^{(3)} \end{cases} \quad (16)$$

This is the third key idea of the present paper which makes it possible to eventually provide sufficient conditions for higher order accurate reconstructions. We notice the second and third sub-equations of Eq. (16) are based on the information on  $S_{i-1} = \{\Omega_{i-2}, \Omega_{i-1}, \Omega_i\}$  and  $S_{i+1} = \{\Omega_i, \Omega_{i+1}, \Omega_{i+2}\}$  respectively. Since the related terms such as  $C_{i-1}^{(1)}|_{step\ 1}$  are pre-computed and stored in Eq. (16), it does not have to deal with information defined on  $S_{i-1}$  and  $S_{i+1}$  directly. Therefore, this method is operationally compact. The difficulty in Eq. (16) is that the second and third sub-equations of Eq. (16) cannot be used directly to reconstruct  $u_i(x)$  since  $C_{i-1}^{(l)}$  and  $C_{i+1}^{(l)}$  are the coefficients for the reconstruction polynomials on  $\Omega_{i-1}$  and  $\Omega_{i+1}$  respectively. Fortunately, for a sufficiently smooth  $u(x)$ ,  $C_{i-1}^{(l)}$  and  $C_{i+1}^{(l)}$  can be represented by  $C_i^{(l)}$  with Taylor expansion and Eq. (2), i.e.

$$\begin{aligned} C_{i-1}^{(1)} &= \frac{\partial u}{\partial x} \Big|_{i-1} \cdot h \approx \left( \frac{\partial u}{\partial x} \Big|_i + \frac{\partial^2 u}{\partial x^2} \Big|_i h + \frac{\partial^3 u}{\partial x^3} \Big|_i \frac{h^2}{2} \right) \cdot h = C_i^{(1)} - 2C_i^{(2)} + 3C_i^{(3)} \\ C_{i-1}^{(2)} &= \frac{\partial^2 u}{\partial x^2} \Big|_{i-1} \cdot \frac{h}{2} \approx \left( \frac{\partial^2 u}{\partial x^2} \Big|_i - \frac{\partial^3 u}{\partial x^3} \Big|_i h \right) \cdot \frac{h}{2} = C_i^{(2)} - 3C_i^{(3)} \\ C_{i-1}^{(3)} &= \frac{\partial^3 u}{\partial x^3} \Big|_{i-1} \cdot \frac{h}{6} \approx C_i^{(3)} \end{aligned}$$

and

$$\begin{aligned} C_{i+1}^{(1)} &= \frac{\partial u}{\partial x} \Big|_{i+1} \cdot h \approx \left( \frac{\partial u}{\partial x} \Big|_i + \frac{\partial^2 u}{\partial x^2} \Big|_i h + \frac{\partial^3 u}{\partial x^3} \Big|_i \frac{h^2}{2} \right) \cdot h = C_i^{(1)} + 2C_i^{(2)} + 3C_i^{(3)} \\ C_{i+1}^{(2)} &= \frac{\partial^2 u}{\partial x^2} \Big|_{i+1} \cdot \frac{h}{2} \approx \left( \frac{\partial^2 u}{\partial x^2} \Big|_i + \frac{\partial^3 u}{\partial x^3} \Big|_i h \right) \cdot \frac{h}{2} = C_i^{(2)} + 3C_i^{(3)} \\ C_{i+1}^{(3)} &= \frac{\partial^3 u}{\partial x^3} \Big|_{i+1} \cdot \frac{h}{6} \approx C_i^{(3)}. \end{aligned}$$

The above technique is called the continuation technique (CT) in the next sub-section, which is the fourth key idea of MSR. Using this technique, Eq. (16) can be transformed into

$$\begin{cases} C_i^{(1)} + 0C_i^{(2)} + \frac{5}{4}C_i^{(3)} = C_i^{(1)}|_{step\ 1} \\ C_i^{(1)} - 2C_i^{(2)} + \frac{17}{4}C_i^{(3)} = C_{i-1}^{(1)}|_{step\ 1} \\ C_i^{(1)} + 2C_i^{(2)} + \frac{17}{4}C_i^{(3)} = C_{i+1}^{(1)}|_{step\ 1} \end{cases} \quad (17)$$

Eq. (17) is the new reconstruction relations. It is possible to calculate all unknowns of the cubic reconstruction by solving Eq. (17) in 1D case. However, it is not always possible in 2D and 3D cases. In the present MSR scheme, in each new step, the PIT is applied to solve the coefficients of polynomial one degree higher than the previous step. In this case, they are  $C_i^{(1)}$  and  $C_i^{(2)}$ . To this end, Eq. (17) is rewritten as

$$\begin{cases} C_i^{(1)} = C_i^{(1)}|_{step\ 1} - \frac{5}{4}C_i^{(3)} \\ C_i^{(1)} - 2C_i^{(2)} = C_{i-1}^{(1)}|_{step\ 1} - \frac{17}{4}C_i^{(3)} \\ C_i^{(1)} + 2C_i^{(2)} = C_{i+1}^{(1)}|_{step\ 1} - \frac{17}{4}C_i^{(3)} \end{cases}$$

It is again possible to calculate the least square solution of  $C_i^{(1)}$  and  $C_i^{(2)}$  since the above system of linear equations is overdetermined. The result is

$$\begin{cases} C_i^{(1)} = \frac{1}{3}(C_i^{(1)}|_{step\ 1} + C_{i-1}^{(1)}|_{step\ 1} + C_{i+1}^{(1)}|_{step\ 1}) - \frac{13}{4}C_i^{(3)} \\ C_i^{(2)} = \frac{1}{4}(C_{i+1}^{(1)}|_{step\ 1} - C_{i-1}^{(1)}|_{step\ 1}) \end{cases}$$

which is further denoted as

$$\begin{cases} C_i^{(1)} = C_i^{(1)}|_{\text{step } 2} - \frac{13}{4}C_i^{(3)} \\ C_i^{(2)} = C_i^{(2)}|_{\text{step } 2} \end{cases} \quad (18)$$

using the definition

$$\begin{aligned} C_i^{(1)}|_{\text{step } 2} &= \frac{1}{3}(C_i^{(1)}|_{\text{step } 1} + C_{i-1}^{(1)}|_{\text{step } 1} + C_{i+1}^{(1)}|_{\text{step } 1}) \\ C_i^{(2)}|_{\text{step } 2} &= \frac{1}{4}(C_{i+1}^{(1)}|_{\text{step } 1} - C_{i-1}^{(1)}|_{\text{step } 1}). \end{aligned}$$

Again the  $C_i^{(3)}$  term can be neglected to obtain the quadratic reconstruction, which is however retained so that Eq. (18) can be used as the relations for the final cubic reconstruction.

In the third step, Eq. (18) evaluated on cells belonging to the compact stencil of Eq. (9) is used as the new reconstruction relations. In this case, there are 6 equations in the reconstruction relations. After applying CT, these equations are solved using least squares for all unknown coefficients of the cubic reconstruction. The details are not presented since they are basically the same as the second step.

It is easy to observe that, during the implementation of MSR procedure, the cells involved in the reconstruction will increase accordingly in every new step. However, there is no need to explicitly handle the stencil and the procedure is operationally compact. This property is sufficient to cure the shortcomings associated with the large stencil problem.

## 2.2. 1D multi-step reconstruction

In this sub-section, the 1D cubic reconstruction using the MSR technique will be formally introduced without the restriction of uniform grids. The purpose of this section is to introduce MSR using matrix-vector operations which can be extended into the 2D and 3D cases more straightforwardly. For the case of  $p = 3$ , we denote  $\mathbf{C}_i = [C_i^{(1)}, C_i^{(2)}, C_i^{(3)}]^T$  as the coefficient vector so that Eq. (6) can be written in the matrix form

$$u_i(x) - \bar{u}_i = [\phi_{1,i}, \phi_{2,i}, \phi_{3,i}]\mathbf{C}_i. \quad (19)$$

In what follows, the 4th order accurate MSR is described to determine the unknown coefficient vector  $\mathbf{C}_i$ . Generally speaking, to reconstruct a degree  $p$  polynomial, a  $p$ -step of reconstruction is needed.

### Step 1

Because of the use of the zero-mean basis, Eq. (19) conserve the cell average automatically. In the first step, the following reconstruction conditions can be obtained using Eq. (8),

$$\begin{bmatrix} \langle \phi_{1,i} \rangle^{i-1} & \langle \phi_{2,i} \rangle^{i-1} & \langle \phi_{3,i} \rangle^{i-1} \\ \langle \phi_{1,i} \rangle^{i+1} & \langle \phi_{2,i} \rangle^{i+1} & \langle \phi_{3,i} \rangle^{i+1} \end{bmatrix} \mathbf{C}_i = \begin{bmatrix} \bar{u}_{i-1} - \bar{u}_i \\ \bar{u}_{i+1} - \bar{u}_i \end{bmatrix}. \quad (20)$$

Eq. (20) can be written in the concise form as

$$A_i \mathbf{C}_i = \boldsymbol{\alpha}_i, \quad (21)$$

where

$$\begin{bmatrix} \langle \phi_{1,i} \rangle^{i-1} & \langle \phi_{2,i} \rangle^{i-1} & \langle \phi_{3,i} \rangle^{i-1} \\ \langle \phi_{1,i} \rangle^{i+1} & \langle \phi_{2,i} \rangle^{i+1} & \langle \phi_{3,i} \rangle^{i+1} \end{bmatrix}, \quad \boldsymbol{\alpha}_i = \begin{bmatrix} \bar{u}_{i-1} - \bar{u}_i \\ \bar{u}_{i+1} - \bar{u}_i \end{bmatrix}.$$

There are 3 unknown coefficients in the vector  $\mathbf{C}_i$ , thus Eq. (21) is underdetermined. Therefore, it is not possible to obtain  $\mathbf{C}_i$  directly. To proceed, here we introduce the so-called partial inversion technique (PIT). Instead of solving for all the unknown coefficients at once, the PIT deals with the coefficient related to linear polynomial i.e.  $C_i^1$ . Correspondingly, matrix  $A_i$  and vector  $\mathbf{C}_i$  are respectively partitioned into two parts: one related to linear polynomial and the other is the rest. Eq. (21) is thus rearranged as

$$\begin{bmatrix} A_{i,1} & A_{i,23} \end{bmatrix} \begin{bmatrix} \mathbf{C}_{i,1} \\ \mathbf{C}_{i,23} \end{bmatrix} = \boldsymbol{\alpha}_i \quad (22)$$

or equivalently

$$A_{i,1} \mathbf{C}_{i,1} = \boldsymbol{\alpha}_i - A_{i,23} \mathbf{C}_{i,23}, \quad (23)$$

where

$$A_{i,1} = \begin{bmatrix} \langle \phi_{1,i} \rangle^{i-1} \\ \langle \phi_{1,i} \rangle^{i+1} \end{bmatrix}, \quad A_{i,23} = \begin{bmatrix} \langle \phi_{2,i} \rangle^{i-1} & \langle \phi_{3,i} \rangle^{i-1} \\ \langle \phi_{2,i} \rangle^{i+1} & \langle \phi_{3,i} \rangle^{i+1} \end{bmatrix}, \quad \mathbf{C}_{i,1} = [\mathbf{C}_i^{(1)}]^T, \quad \mathbf{C}_{i,23} = [\mathbf{C}_i^{(2)} \quad \mathbf{C}_i^{(3)}]^T.$$

Then,  $A_{i,1}^+ \equiv (A_{i,1}^T A_{i,1})^{-1} A_{i,1}^T$ , the Moore-Penrose inverse of  $A_{i,1}$ , is firstly calculated. One purpose of introducing  $A_{i,1}^+$  is to perform linear reconstruction. Indeed, if the contribution of higher order terms corresponding to  $A_{i,23}$  is neglected, the use of the least-square inversion technique leads to

$$\mathbf{C}_{i,1}|_{\text{step 1}} = A_{i,1}^+ \boldsymbol{\alpha}_i,$$

which is the traditional linear k-exact reconstruction. In practice, we retain the high order terms and use the least squares solution of Eq. (23) as the reconstruction relations of the second step. To this end,  $A_{i,1}^+$  is used to pre-multiply Eq. (22) or Eq. (23) to obtain the regularized reconstruction relations (RRR, in plural number)

$$\begin{bmatrix} A_{i,1}^+ A_{i,1} & A_{i,1}^+ A_{i,23} \end{bmatrix} \mathbf{C}_i = A_{i,1}^+ \boldsymbol{\alpha}_i \quad (24)$$

or

$$A_{i,1}^+ A_i \mathbf{C}_i = A_{i,1}^+ \boldsymbol{\alpha}_i. \quad (25)$$

We notice that Eq. (24) or (25) is the linear mapping of the original reconstruction relation Eq. (21). This property is important that guarantees the k-exactness of the proposed reconstruction procedure. The least squares operation in Eq. (25) is used to reduce the number of the RRR being the number of unknown coefficients of the linear polynomial (or more general, being the number of the lower degree polynomial in PIT as shown in Step 2).

#### Step 2

The second step is the first recursive step of this MSR scheme. It will be described in detail to demonstrate how higher order reconstruction is obtained from lower order ones.

The main idea for achieving higher order reconstruction is to combine the RRR on the current cell (Eq. (25)) and its face-neighboring cells derived in Step 1 to construct new reconstruction relations. The direct realization of this idea leads to

$$\begin{bmatrix} A_{i,1}^+ A_i \mathbf{C}_i \\ A_{i-1,1}^+ A_{i-1} \mathbf{C}_{i-1} \\ A_{i+1,1}^+ A_{i+1} \mathbf{C}_{i+1} \end{bmatrix} = \begin{bmatrix} A_{i,1}^+ \boldsymbol{\alpha}_i \\ A_{i-1,1}^+ \boldsymbol{\alpha}_{i-1} \\ A_{i+1,1}^+ \boldsymbol{\alpha}_{i+1} \end{bmatrix}. \quad (26)$$

These relations cannot be used directly since  $\mathbf{C}_i$ ,  $\mathbf{C}_{i-1}$  and  $\mathbf{C}_{i+1}$  are the unknown coefficients on different cells. To solve this problem, the second technique associated with the MSR, namely the continuation technique (CT) is proposed. In this technique, when the solution  $u(x)$  is smooth,  $\mathbf{C}_j$  ( $j = i - 1$  or  $i + 1$ ) is expressed as the linear transformation of  $\mathbf{C}_i$ , i.e.

$$\mathbf{C}_j = T_{j(\rightarrow i)} \mathbf{C}_i. \quad (27)$$

In Eq. (27),  $T_{j(\rightarrow i)}$  (or  $T_j$  for short) is a  $3 \times 3$  square matrix related to grid sizes. The derivation of Eq. (27) is given in Appendix A by the continuation of the reconstruction polynomial  $u_j(x)$  defined on  $\Omega_j$  onto  $\Omega_i$ , where  $\Omega_j$  is a face-neighboring cell of  $\Omega_i$ . Also, in Appendix A, we prove that if solution  $u$  follows cubic polynomial distribution, Eq. (27) is exact. Substituting Eq. (27) into Eq. (26), we can reach a system of equations only related to  $\mathbf{C}_i$ , i.e.

$$\begin{bmatrix} A_{i,1}^+ A_i \\ A_{i-1,1}^+ A_{i-1} T_{i-1} \\ A_{i+1,1}^+ A_{i+1} T_{i+1} \end{bmatrix} \mathbf{C}_i = \begin{bmatrix} A_{i,1}^+ \boldsymbol{\alpha}_i \\ A_{i-1,1}^+ \boldsymbol{\alpha}_{i-1} \\ A_{i+1,1}^+ \boldsymbol{\alpha}_{i+1} \end{bmatrix}, \quad (28)$$

which is denoted further as

$$B_i \mathbf{C}_i = \boldsymbol{\beta}_i. \quad (29)$$

It is worthwhile to notice that Eq. (29) is also k-exact. Eq. (29) is the new reconstruction relations used in the second step. In this step, the PIT deals with the coefficients related to quadratic polynomial i.e.  $\mathbf{C}_i^{(1)}$  and  $\mathbf{C}_i^{(2)}$ . We partition matrix  $B_i$  and vector  $\boldsymbol{\beta}_i$  into two parts and Eq. (29) represented by partitioned matrices becomes

$$\begin{bmatrix} B_{i,12} & B_{i,3} \end{bmatrix} \begin{bmatrix} \mathbf{C}_{i,12} \\ \mathbf{C}_{i,3} \end{bmatrix} = \boldsymbol{\beta}_i \quad (30)$$

or equivalently

$$B_{i,12} \mathbf{C}_{i,12} = \boldsymbol{\beta}_i - B_{i,3} \mathbf{C}_{i,3}, \quad (31)$$

where  $B_{i,12}$  is the first 2 columns of  $B_i$  corresponding to the linear and quadratic terms,  $B_{i,3}$  is the rest of  $B_i$ , and

$$\mathbf{C}_{i,12} = \begin{bmatrix} C_i^{(1)} & C_i^{(2)} \end{bmatrix}^T, \quad \mathbf{C}_{i,3} = [C_i^{(3)}]^T.$$

As the PIT in the first step, the Moore-Penrose inverse of  $B_{i,12}$  is computed as  $B_{i,12}^+$ . Since there are 3 equations in Eq. (30) or (31), it is sufficient to determine a least squares quadratic reconstruction by neglecting the  $B_{i,3}\mathbf{C}_{i,3}$  term in Eq. (31), which is given by

$$\mathbf{C}_{i,12}|_{\text{step 2}} = B_{i,12}^+ \boldsymbol{\beta}_i.$$

For higher order reconstruction, the  $B_{i,3}\mathbf{C}_{i,3}$  term is retained and the RRR are derived by pre-multiplying Eq. (30) or (31) with  $B_{i,12}^+$ , i.e.

$$B_{i,12}^+ B_{i,3} \mathbf{C}_i = B_{i,12}^+ \boldsymbol{\beta}_i \quad \text{or} \quad \begin{bmatrix} B_{i,12}^+ B_{i,12} & B_{i,12}^+ B_{i,3} \end{bmatrix} \mathbf{C}_i = B_{i,12}^+ \boldsymbol{\beta}_i. \quad (32)$$

*Step 3*

The *Step 3* is the last step for 4th order MSR. The reconstruction relations are provided by the collection of the RRR derived in Eq. (32) of *Step 2* on current cell  $\Omega_i$  and its face-neighboring cells  $\Omega_j$  ( $j = i - 1$  and  $i + 1$ ) as

$$\begin{bmatrix} B_{i,12}^+ B_i \mathbf{C}_i \\ B_{i-1,12}^+ B_{i-1} \mathbf{C}_{i-1} \\ B_{i+1,12}^+ B_{i+1} \mathbf{C}_{i+1} \end{bmatrix} = \begin{bmatrix} B_{i,12}^+ \boldsymbol{\beta}_i \\ B_{i-1,12}^+ \boldsymbol{\beta}_{i-1} \\ B_{i+1,12}^+ \boldsymbol{\beta}_{i+1} \end{bmatrix}.$$

The use of CT leads to

$$\begin{bmatrix} B_{i,12}^+ B_i \\ B_{i-1,12}^+ B_{i-1} T_{i-1} \\ B_{i+1,12}^+ B_{i+1} T_{i+1} \end{bmatrix} \mathbf{C}_i = \begin{bmatrix} B_{i,12}^+ \boldsymbol{\beta}_i \\ B_{i-1,12}^+ \boldsymbol{\beta}_{i-1} \\ B_{i+1,12}^+ \boldsymbol{\beta}_{i+1} \end{bmatrix}, \quad (33)$$

which can be denoted as

$$M_i \mathbf{C}_i = \boldsymbol{\gamma}_i. \quad (34)$$

There are 6 relations in Eq. (33) or (34). It is sufficient to perform the cubic reconstruction using the least squares. The result is

$$\mathbf{C}_i = M_i^+ \boldsymbol{\gamma}_i,$$

where  $M_i^+$  is the Moore-Penrose inverse of  $M_i$ . Since we use the cubic reconstruction to demonstrate the MSR procedure, the PIT is not needed in the last step.

**Remark 1.** It can be proved that all reconstruction relations and corresponding RRR presented in *Steps 1–3* are exactly satisfied when solution  $u(x)$  follows cubic polynomial distribution. Therefore, the proposed MSR is k-exact. The detailed proof is presented in Appendix B. The k-exactness of the present procedure ensures that the spatially 4th order accuracy can be achieved theoretically for the FV schemes using the cubic reconstructions.

**Remark 2.** The RRR can be weighted to change relative importance of different relations. For example, Eqs. (28) and (33) can be changed respectively to

$$\begin{bmatrix} A_{i,1}^+ A_i \\ \omega A_{i-1,1}^+ A_{i-1} T_{i-1} \\ \omega A_{i+1,1}^+ A_{i+1} T_{i+1} \end{bmatrix} \mathbf{C}_i = \begin{bmatrix} A_{i,1}^+ \boldsymbol{\alpha}_i \\ \omega A_{i-1,1}^+ \boldsymbol{\alpha}_{i-1} \\ \omega A_{i+1,1}^+ \boldsymbol{\alpha}_{i+1} \end{bmatrix} \quad (35)$$

and

$$\begin{bmatrix} B_{i,12}^+ B_i \\ \omega B_{i-1,12}^+ B_{i-1} T_{i-1} \\ \omega B_{i+1,12}^+ B_{i+1} T_{i+1} \end{bmatrix} \mathbf{C}_i = \begin{bmatrix} B_{i,12}^+ \boldsymbol{\beta}_i \\ \omega B_{i-1,12}^+ \boldsymbol{\beta}_{i-1} \\ \omega B_{i+1,12}^+ \boldsymbol{\beta}_{i+1} \end{bmatrix}. \quad (36)$$

The weight is usually chosen as  $\omega \in (0, 1]$  since the RRR of the central cell should be more important than those of the neighboring cells. It is trivial to show that the introduction of the weights does not affect the k-exactness of the reconstruction procedure. The impact of the weights will be discussed in Section 2.3.



**Remark 3.** Steps 1–3 only demonstrate a 4th order accurate cubic reconstruction procedure with MSR. The recursive Steps 2 and 3 are used to raise degree of reconstruction by 1, respectively. When a 5th order accurate reconstruction is required, we use quartic polynomial i.e.  $p = 4$  in Eq. (1) and the corresponding vector  $\mathbf{C}_i = [C_i^{(1)} \ C_i^{(2)} \ C_i^{(3)} \ C_i^{(4)}]^T$  is to be determined. In this case, the reconstructions with 4 stages can be used, in which the first and the second stages are basically the same as the cubic reconstruction, the third stage is added to construct the RRR for quartic reconstruction, and the last (fourth) stage is similar to the third stage of the cubic reconstruction. It is then clear that arbitrary order reconstruction can be easily achieved by repeating the recursive steps. In general, the reconstruction for  $n$ -th order accurate FV schemes requires  $n - 1$  steps with Step 2 to Step  $n - 1$  implemented recursively.

### 2.3. Fourier analysis

In this section, Fourier analysis of the semi-discretized FV scheme using the MSR is presented for the discussion of dispersion and dissipation properties of the proposed scheme. The governing equation is a scalar linear wave equation

$$\frac{\partial u}{\partial t} + \frac{\partial f}{\partial x} = 0, \quad (37)$$

where  $f = au$  and  $a$  is a positive constant. For simplicity, we assume that the grids are uniform i.e.  $h_i \equiv h$ . The integral form of Eq. (37) on cell  $\Omega_i$  is

$$\frac{\partial \bar{u}_i}{\partial t} = -\frac{1}{h}(f_{i+1/2} - f_{i-1/2}), \quad (38)$$

where  $f_{i+1/2}$  is exact flux. The semi-discrete scheme of Eq. (38) is

$$\frac{\partial \bar{u}_i}{\partial t} = -\frac{1}{h}(\hat{f}_{i+1/2} - \hat{f}_{i-1/2}), \quad (39)$$

where  $\hat{f}_{i+1/2}$  is numerical flux. In the analysis, upwind fluxes are used such that

$$\hat{f}_{i+1/2} = au_{i+1/2}^L, \quad (40)$$

where  $u_{i+1/2}^L$  denotes approximation of  $u(x)$  at  $x_{i+1/2}$  computed using the MSR on the left-side cell  $\Omega_i$ .

Fourier analysis is presented to study the spectral behavior of FV schemes using MSR. A single wave  $u(x, t) = A_m(t)e^{ik_mx}$  with a wavenumber  $k_m$  is considered as the solution in the analysis, leading to the cell average

$$\bar{u}_i = \frac{A_m}{ik_m h}(e^{ik_mx_{i+1/2}} - e^{ik_mx_{i-1/2}}) \quad (41)$$

and exact flux

$$f_{i+1/2} = aA_me^{ik_mx_{i+1/2}}$$

respectively. These formulations are then introduced to the integral form of Eq. (38) which gives

$$\frac{\partial A_m}{\partial t} + ik_m a A_m = 0.$$

Correspondingly, using Eq. (41) in the MSR, the semi-discrete scheme Eq. (39) with the numerical flux Eq. (40) becomes

$$\frac{\partial A_m}{\partial t} + ik'_m a A_m = 0,$$

where in Fourier space

$$\frac{k'_m}{k_m} = \frac{\hat{f}_{i+1/2} - \hat{f}_{i-1/2}}{f_{i+1/2} - f_{i-1/2}}.$$

The wavenumber  $k_m$  and  $k'_m$  can be scaled as

$$\kappa = k_m h, \quad \kappa' = k'_m h,$$

where  $\kappa$  is called scaled wavenumber and  $\kappa'$  is called modified wavenumber. The relation of these two wavenumbers can be written as

$$\kappa' = \frac{\hat{f}_{i+1/2} - \hat{f}_{i-1/2}}{f_{i+1/2} - f_{i-1/2}} \kappa.$$

In the finite volume schemes,  $\kappa'$  is in general a complex number whose real part is associated with the dispersion error and imaginary part is associated with the dissipation error. It can be calculated as a function of the scaled wavenumber  $\kappa$ . The specific forms of  $\kappa'$  for 2nd to 4th order accurate reconstructions are given below.

The 2nd order accurate MSR:

$$\begin{aligned}\operatorname{Re}(\kappa') &= \frac{3}{2} \sin(\kappa) - \frac{1}{4} \sin(2\kappa), \\ \operatorname{Im}(\kappa') &= -\frac{3}{4} + \cos(\kappa) - \frac{1}{4} \cos(2\kappa).\end{aligned}$$

The 3rd order accurate MSR:

$$\begin{aligned}\operatorname{Re}(\kappa') &= \frac{(69 + 78\omega^2) \sin(\kappa) + (-12 + 24\omega^2) \sin(2\kappa) + (1 - 10\omega^2) \sin(3\kappa)}{48(1 + 2\omega^2)}, \\ \operatorname{Im}(\kappa') &= \frac{-34 - 92\omega^2 + (47 + 106\omega^2) \cos(\kappa) + (-14 - 4\omega^2) \cos(2\kappa) + (1 - 10\omega^2) \cos(3\kappa)}{48(1 + 2\omega^2)}.\end{aligned}$$

The 4th order accurate MSR:

$$\begin{aligned}\operatorname{Re}(\kappa') &= \frac{1}{q_0} (q_1 \sin(\kappa) + q_2 \sin(2\kappa) + q_3 \sin(3\kappa) + q_4 \sin(4\kappa)), \\ \operatorname{Im}(\kappa') &= \frac{1}{q_0} (q_5 + q_6 \cos(\kappa) + q_7 \cos(2\kappa) + q_8 \cos(3\kappa) + q_9 \cos(4\kappa)),\end{aligned}$$

where

$$\begin{cases} q_0 = 192(1 + \omega^2)(1 + 2\omega^2)^2 \\ q_1 = 302 + 1296\omega^2 + 1648\omega^4 + 1200\omega^6 \\ q_2 = -66 - 100\omega^2 + 288\omega^4 - 224\omega^6 \\ q_3 = 6 - 80\omega^2 - 336\omega^4 - 16\omega^6 \\ q_4 = 1 + 26\omega^2 + 80\omega^4 + 16\omega^6 \\ q_5 = -125 - 730\omega^2 - 1360\omega^4 - 560\omega^6 \\ q_6 = 184 + 1004\omega^2 + 1760\omega^4 + 784\omega^6 \\ q_7 = -68 - 256\omega^2 - 256\omega^4 - 224\omega^6 \\ q_8 = 8 - 44\omega^2 - 224\omega^4 - 16\omega^6 \\ q_9 = 1 + 26\omega^2 + 80\omega^4 + 16\omega^6 \end{cases}.$$

There is a parameter  $\omega$  that is the weight introduced in Eqs. (35) and (36). In the present paper, we usually choose  $\omega = 1$ . A smaller value of  $\omega$  can be adopted to emphasize the contribution of the central cell. An optimization procedure of  $\omega$  is implemented by minimizing cost function [38,43]

$$E = \frac{1}{e^{\nu\pi}} \int_0^\pi e^{\nu(\pi-\kappa)} (\operatorname{Re}(\kappa') - \kappa)^2 d\kappa. \quad (42)$$

We choose  $\nu = 4$  in Eq. (42) for 3rd and 4th order accurate schemes and find that the cost function is monotonically increasing with  $\omega$  in  $(0, 1]$ . It indicates that the smaller the weight  $\omega$ , the smaller the dispersion error. On the other hand, a very small  $\omega$  tends to make the reconstruction singular. In the present paper,  $\omega = 0.2$  is chosen as an optimized value since the dispersion relation changes very little when  $\omega$  is smaller than 0.2.

In Fig. 1a, the real parts of  $\kappa'$  are plotted for the 2nd, 3rd and 4th order accurate MSRs. The 4th order accurate central difference scheme (C4) [44] and the 4th order accurate CLS scheme [38] is also presented for comparison. It is evident that higher order schemes produce smaller dispersion errors. Compared to the standard 4th order central difference scheme, FV schemes based on the cubic MSR stay closer to the exact dispersion relations over a wider range of wavenumber. The optimized 4th order accurate reconstruction with  $\omega = 0.2$  is better than the standard case with  $\omega = 1$  and closed to CLS scheme. In Fig. 1b, the imaginary parts of  $\kappa'$  are plotted for the 2nd, 3rd, 4th order accurate MSR schemes, the C4 scheme and the CLS scheme to compare the dissipation properties of different schemes. It can be noted that the increase of the accuracy reduces dissipation errors in the low wavenumber range, but slightly affects intermediate wavenumber range. The measure of phase error  $\operatorname{Re}(\kappa')/\kappa - 1$  is more intuitive to show the phase speed. In Fig. 2, this information for different schemes is also presented. The improvement in the dispersion property for the optimized MSR scheme is clearly shown.

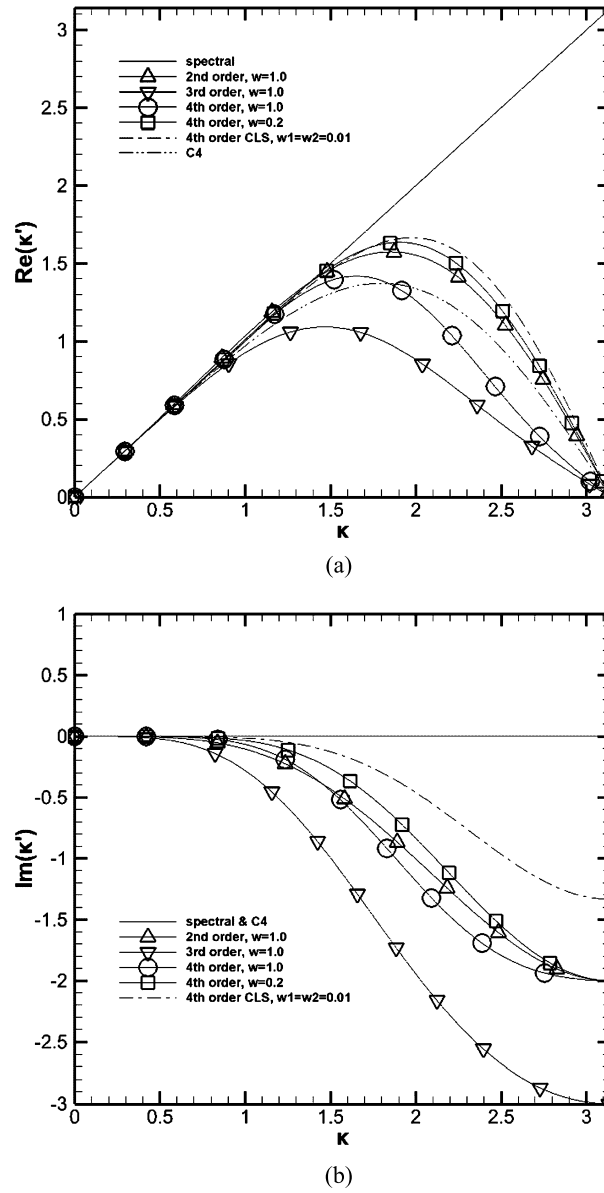


Fig. 1. Dispersion and dissipation properties of the 2nd to 4th order MSR schemes.

### 3. High order compact multi-step reconstruction for FV schemes: the 2D case

#### 3.1. Notations

In the 2D case, we are interested in the FV method on the unstructured triangular grids. The computational domain  $\Omega$  is composed of a collection of  $N$  non-overlapping space filling triangles, i.e.

$$\Omega = \bigcup_{i=1}^N \Omega_i,$$

where  $\Omega_i$  is the  $i$ -th cell. For a specific triangular cell  $\Omega_i$ , the boundary is composed of 3 edges or interfaces

$$\partial\Omega_i = \bigcup_{m=1}^3 I_m.$$

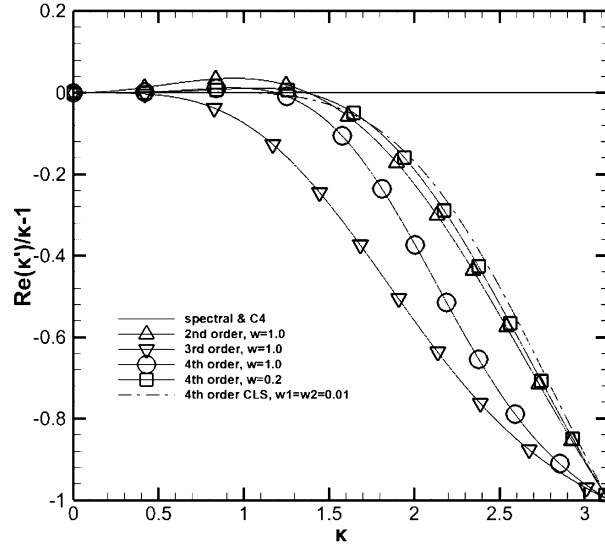


Fig. 2. Dispersion errors of the 2nd to 4th order MSR schemes.

Supposing 3 nodes (vertices) of the specific cell  $\Omega_i$  is point 1, 2, 3 and coordinates of those points are  $(X_1, Y_1)$ ,  $(X_2, Y_2)$ ,  $(X_3, Y_3)$  respectively (capital letters are used here to be distinguished from coordinates of cell centers). The volume of  $\Omega_i$  is computed using

$$|\Omega_i| = \frac{1}{2} [(X_1 - X_2)(Y_1 + Y_2) + (X_2 - X_3)(Y_2 + Y_3) + (X_3 - X_1)(Y_3 + Y_1)].$$

The nodes have to be numbered in the anti-clockwise direction to obtain a positive volume. The center of  $\Omega_i$  is defined as

$$(x_i, y_i) = \left( \frac{X_1 + X_2 + X_3}{3}, \frac{Y_1 + Y_2 + Y_3}{3} \right).$$

We denote the  $i$ -th cell average of the dependent variable  $u(x, y)$  as

$$\bar{u}_i = \frac{1}{|\Omega_i|} \int_{\Omega_i} u(x, y) d\Omega. \quad (43)$$

In the reconstruction procedure, the variable  $u(x, y)$  is approximated within each cell  $\Omega_i$  by a local polynomial  $u_i(x, y)$  of the form:

$$u_i(x, y) = \bar{u}_i + \sum_{l=1}^{NOC(p)} C_i^{(l)} \phi_{l,i}(x, y), \quad (44)$$

where  $NOC(p)$  is the number of unknown coefficients for degree  $p$  polynomial e.g.  $NOC(1) = 2$ ,  $NOC(2) = 5$ ,  $NOC(3) = 9$ . In this paper, 4th order accurate MSR method is presented and we take basis function  $\phi_{l,i}$  as the zero-mean basis, i.e.

$$\begin{aligned} \phi_{1,i} &= (x - x_i)/h_i \\ \phi_{2,i} &= (y - y_i)/h_i \\ \phi_{3,i} &= (x - x_i)^2/h_i^2 - \langle (x - x_i)^2/h_i^2 \rangle^i \\ \phi_{4,i} &= (x - x_i)(y - y_i)/h_i^2 - \langle (x - x_i)(y - y_i)/h_i^2 \rangle^i \\ \phi_{5,i} &= (y - y_i)^2/h_i^2 - \langle (y - y_i)^2/h_i^2 \rangle^i \\ \phi_{6,i} &= (x - x_i)^3/h_i^3 - \langle (x - x_i)^3/h_i^3 \rangle^i \\ \phi_{7,i} &= (x - x_i)^2(y - y_i)/h_i^3 - \langle (x - x_i)^2(y - y_i)/h_i^3 \rangle^i \\ \phi_{8,i} &= (x - x_i)(y - y_i)^2/h_i^3 - \langle (x - x_i)(y - y_i)^2/h_i^3 \rangle^i \\ \phi_{9,i} &= (y - y_i)^3/h_i^3 - \langle (y - y_i)^3/h_i^3 \rangle^i, \end{aligned}$$

where

$$\langle f(x, y) \rangle^i = \frac{1}{|\Omega_i|} \int_{\Omega_i} f(x, y) d\Omega.$$

$C_i^{(l)}$  can be considered as the scaled derivative of  $u_i(\mathbf{x})$ , as shown below

$$\begin{aligned} C_i^{(1)} &= \frac{\partial u}{\partial x} \Big|_i \cdot h_i, & C_i^{(2)} &= \frac{\partial u}{\partial y} \Big|_i \cdot h_i, \\ C_i^{(3)} &= \frac{\partial^2 u}{\partial x^2} \Big|_i \cdot \frac{h_i^2}{2!}, & C_i^{(4)} &= \frac{\partial^2 u}{\partial x \partial y} \Big|_i \cdot h_i^2, & C_i^{(5)} &= \frac{\partial^2 u}{\partial y^2} \Big|_i \cdot \frac{h_i^2}{2!}, \\ C_i^{(6)} &= \frac{\partial^3 u}{\partial x^3} \Big|_i \cdot \frac{h_i^3}{3!}, & C_i^{(7)} &= \frac{\partial^3 u}{\partial x^2 \partial y} \Big|_i \cdot \frac{h_i^3}{2!}, & C_i^{(8)} &= \frac{\partial^3 u}{\partial x \partial y^2} \Big|_i \cdot \frac{h_i^3}{2!}, & C_i^{(9)} &= \frac{\partial^3 u}{\partial y^3} \Big|_i \cdot \frac{h_i^3}{3!}. \end{aligned}$$

For convenience, we define  $\mathbf{C}_i = [C_i^{(1)} \ C_i^{(2)} \ \dots \ C_i^{(9)}]^T$  as the coefficient vector so that Eq. (44) can be written in the matrix form

$$u_i(x, y) - \bar{u}_i = [\phi_{1,i} \ \phi_{2,i} \ \dots \ \phi_{9,i}] \mathbf{C}_i. \quad (45)$$

In what follows, the 4th order accurate MSR is described to determine the unknown coefficient vector  $\mathbf{C}_i$ . Generally speaking, to reconstruct a degree  $p$  polynomial, a  $p$ -step of reconstruction is needed.

### 3.2. 2D multi-step reconstruction

The reconstruction procedure on 2D grids is essentially same as that in Section 1. In this section, a 4th order accurate MSR is presented. The boundary treatment and the selection of weights are also studied to demonstrate the differences from the 1D case.

#### Step 1

For a triangular cell  $\Omega_i$ , it has 3 cells  $\Omega_{j_1}, \Omega_{j_2}, \Omega_{j_3}$  as its direct neighbors. The reconstruction conditions in the 2D case for the reconstruction of  $u_i(x, y)$  on  $\Omega_i$  are

$$\sum_{l=1}^9 C_i^{(l)} \langle \phi_{l,i}(x, y) \rangle^j = \bar{u}_j - \bar{u}_i, \quad j = j_1, j_2, j_3 \quad (46)$$

These reconstruction conditions can be written in matrix form as

$$\begin{bmatrix} \langle \phi_{1,i} \rangle^{j_1} & \langle \phi_{2,i} \rangle^{j_1} & \dots & \langle \phi_{9,i} \rangle^{j_1} \\ \langle \phi_{1,i} \rangle^{j_2} & \langle \phi_{2,i} \rangle^{j_2} & \dots & \langle \phi_{9,i} \rangle^{j_2} \\ \langle \phi_{1,i} \rangle^{j_3} & \langle \phi_{2,i} \rangle^{j_3} & \dots & \langle \phi_{9,i} \rangle^{j_3} \end{bmatrix} \mathbf{C}_i = \begin{bmatrix} \bar{u}_{j_1} - \bar{u}_i \\ \bar{u}_{j_2} - \bar{u}_i \\ \bar{u}_{j_3} - \bar{u}_i \end{bmatrix}$$

or in more compact form

$$A_i \mathbf{C}_i = \boldsymbol{\alpha}_i. \quad (47)$$

There are 9 unknown coefficients in the vector  $\mathbf{C}_i$ , thus the 3-equation system Eq. (47) is underdetermined. By using the PIT, Eq. (47) is partitioned as

$$\begin{bmatrix} A_{i,1} & A_{i,23} \end{bmatrix} \begin{bmatrix} \mathbf{C}_{i,1} \\ \mathbf{C}_{i,23} \end{bmatrix} = \boldsymbol{\alpha}_i \quad (48)$$

or equivalently

$$A_{i,1} \mathbf{C}_{i,1} = \boldsymbol{\alpha}_i - A_{i,23} \mathbf{C}_{i,23}, \quad (49)$$

where

$$\begin{aligned} A_{i,1} &= \begin{bmatrix} \langle \phi_{1,i} \rangle^{j_1} & \langle \phi_{2,i} \rangle^{j_1} \\ \langle \phi_{1,i} \rangle^{j_2} & \langle \phi_{2,i} \rangle^{j_2} \\ \langle \phi_{1,i} \rangle^{j_3} & \langle \phi_{2,i} \rangle^{j_3} \end{bmatrix}, & A_{i,23} &= \begin{bmatrix} \langle \phi_{3,i} \rangle^{j_1} & \dots & \langle \phi_{9,i} \rangle^{j_1} \\ \langle \phi_{3,i} \rangle^{j_2} & \dots & \langle \phi_{9,i} \rangle^{j_2} \\ \langle \phi_{3,i} \rangle^{j_3} & \dots & \langle \phi_{9,i} \rangle^{j_3} \end{bmatrix} \\ \mathbf{C}_{i,1} &= [C_i^{(1)} \ C_i^{(2)}]^T, & \mathbf{C}_{i,23} &= [C_i^{(3)} \ \dots \ C_i^{(9)}]^T. \end{aligned} \quad (50)$$

In Eqs. (48), (49) and (50), the components of  $\mathbf{C}_{i,1}$  are the linear terms, and the components of  $\mathbf{C}_{i,23}$  are higher order terms. The RRR are the least square solution for  $\mathbf{C}_{i,1}$  when  $\mathbf{C}_{i,23}$  is treated as the right-hand-side of Eq. (49) but remain unsolved. These relations are

$$A_{i,1}^+ A_i \mathbf{C}_i = A_{i,1}^+ \boldsymbol{\alpha}_i, \quad (51)$$

where  $A_{i,1}^+$  represents the Moore-Penrose inverse of  $A_{i,1}$ .

### Step 2

We use CT to express the vector of the unknown coefficients  $\mathbf{C}_j$  on  $\Omega_j$  in terms of that on  $\Omega_i$ , i.e.

$$\mathbf{C}_j = T_{j(\rightarrow i)} \mathbf{C}_i, \quad (52)$$

where  $\Omega_j$  is one of face neighboring cells of  $\Omega_i$ , and  $T_{j(\rightarrow i)}$  ( $T_j$  for short) is a  $9 \times 9$  transformation matrix whose detailed form is presented in Appendix A. Applying Eq. (52) to the RRR defined on  $\Omega_j$  ( $j = j_1, j_2, j_3$ ), we obtain the reconstruction relations of Step 2

$$\begin{bmatrix} A_{i,1}^+ A_i \\ A_{j_1,1}^+ A_{j_1} T_{j_1} \\ A_{j_2,1}^+ A_{j_2} T_{j_2} \\ A_{j_3,1}^+ A_{j_3} T_{j_3} \end{bmatrix} \mathbf{C}_i = \begin{bmatrix} A_{i,1}^+ \boldsymbol{\alpha}_i \\ A_{j_1,1}^+ \boldsymbol{\alpha}_{j_1} \\ A_{j_2,1}^+ \boldsymbol{\alpha}_{j_2} \\ A_{j_3,1}^+ \boldsymbol{\alpha}_{j_3} \end{bmatrix}, \quad (53)$$

which can be denoted as

$$B_i \mathbf{u}_i = \boldsymbol{\beta}_i. \quad (54)$$

Applying the PIT to Eq. (54), we partition matrix  $B_i$  and vector  $\mathbf{C}_i$  into two parts as

$$\begin{bmatrix} B_{i,12} & B_{i,3} \end{bmatrix} \begin{bmatrix} \mathbf{C}_{i,12} \\ \mathbf{C}_{i,3} \end{bmatrix} = \boldsymbol{\beta}_i$$

or equivalently

$$B_{i,12} \mathbf{C}_{i,12} = \boldsymbol{\beta}_i - B_{i,3} \mathbf{C}_{i,3}, \quad (55)$$

where  $B_{i,12}$  is the first 5 columns of  $B_i$  corresponding to the linear and quadratic terms,  $B_{i,3}$  is the rest of  $B_i$  and

$$\mathbf{C}_{i,12} = \begin{bmatrix} C_i^{(1)} & \dots & C_i^{(5)} \end{bmatrix}^T, \quad \mathbf{C}_{i,3} = \begin{bmatrix} C_i^{(6)} & \dots & C_i^{(9)} \end{bmatrix}^T.$$

There are generally  $2 \times 4 = 8$  equations in Eq. (55) for triangular grids while the number of unknown coefficients of quadratic polynomial is 5. This means the least-square solution to determine  $\mathbf{C}_{i,12}$  is applicable. Retaining  $\mathbf{C}_{i,3}$  on the right-hand-side of (55), we obtain the least squares solution for  $\mathbf{C}_{i,12}$

$$B_{i,12}^+ B_{i,12} \mathbf{C}_{i,12} = B_{i,12}^+ \boldsymbol{\beta}_i - B_{i,12}^+ B_{i,3} \mathbf{C}_{i,3}$$

or

$$B_{i,12}^+ B_{i,3} \mathbf{C}_i = B_{i,12}^+ \boldsymbol{\beta}_i, \quad (56)$$

which are the RRR of Step 2.

### Step 3

The combination of the RRR on current and face-neighboring cells and the application of CT result in the reconstruction relations of Step 3

$$\begin{bmatrix} B_{i,12}^+ B_i \\ B_{j_1,12}^+ B_{j_1} T_{j_1} \\ B_{j_2,12}^+ B_{j_2} T_{j_2} \\ B_{j_3,12}^+ B_{j_3} T_{j_3} \end{bmatrix} \mathbf{C}_i = \begin{bmatrix} B_{i,12}^+ \boldsymbol{\beta}_i \\ B_{j_1,12}^+ \boldsymbol{\beta}_{j_1} \\ B_{j_2,12}^+ \boldsymbol{\beta}_{j_2} \\ B_{j_3,12}^+ \boldsymbol{\beta}_{j_3} \end{bmatrix}, \quad (57)$$

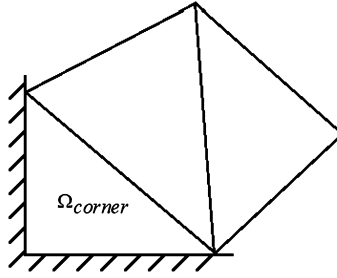
which can be denoted as

$$M_i \mathbf{C}_i = \boldsymbol{\gamma}_i. \quad (58)$$

For triangular grids, there are  $5 \times 4 = 20$  equations in Eq. (58) and it is sufficient to solve the vector of unknown coefficients of the cubic reconstruction polynomial using the least-squares technique, i.e.

$$\mathbf{C}_i = M_i^+ \boldsymbol{\gamma}_i,$$

where  $M_i^+$  is the Moore-Penrose inverse of  $M_i$ .

Fig. 3. Diagram of a corner cell  $\Omega_{corner}$ .

**Remark 4.** Remark 1 in Section 2 introduces probability of improving MSR schemes by combining weighted RRRs. Different from the 1D case on uniform grids, the distance between the current and neighboring cells should be considered for the choice of weights on a multi-dimensional mesh. Eq. (53) and Eq. (57) are thus rewritten as

$$\begin{bmatrix} A_{i,1}^+ A_i \\ \omega_{j_1} A_{j_1,1}^+ A_{j_1} T_{j_1} \\ \omega_{j_2} A_{j_2,1}^+ A_{j_2} T_{j_2} \\ \omega_{j_3} A_{j_3,1}^+ A_{j_3} T_{j_3} \end{bmatrix} \mathbf{C}_i = \begin{bmatrix} A_{i,1}^+ \boldsymbol{\alpha}_i \\ \omega_{j_1} A_{j_1,1}^+ \boldsymbol{\alpha}_{j_1} \\ \omega_{j_2} A_{j_2,1}^+ \boldsymbol{\alpha}_{j_2} \\ \omega_{j_3} A_{j_3,1}^+ \boldsymbol{\alpha}_{j_3} \end{bmatrix}$$

$$\begin{bmatrix} B_{i,12}^+ B_i \\ \omega_{j_1} B_{j_1,12}^+ B_{j_1} T_{j_1} \\ \omega_{j_2} B_{j_2,12}^+ B_{j_2} T_{j_2} \\ \omega_{j_3} B_{j_3,12}^+ B_{j_3} T_{j_3} \end{bmatrix} \mathbf{C}_i = \begin{bmatrix} B_{i,12}^+ \boldsymbol{\beta}_i \\ \omega_{j_1} B_{j_1,12}^+ \boldsymbol{\beta}_{j_1} \\ \omega_{j_2} B_{j_2,12}^+ \boldsymbol{\beta}_{j_2} \\ \omega_{j_3} B_{j_3,12}^+ \boldsymbol{\beta}_{j_3} \end{bmatrix},$$

where  $\omega_j \in (0, 1]$ . The weight  $\omega_j$  denotes the relative importance of the relations obtained on  $\Omega_j$  when applied to the reconstruction of  $\Omega_i$ . In the present paper, the weights are chosen as

$$\omega_j = \left( \frac{r_{ij}}{r_{ij}} \right)^\beta$$

with

$$r_{ij} \doteq \left( \sum_{k=1}^3 [(x_j - X_k^{(i)})^2 + (y_j - Y_k^{(i)})^2] \right)^{\frac{1}{2}}$$

where  $(X_k^{(i)}, Y_k^{(i)})$  is the coordinate for the  $k$ th vertex of cell  $\Omega_i$ . The  $r_{ij}$  is called the ‘distance’ from  $\Omega_j$  to  $\Omega_i$ . It can be proved that  $r_{ij}$  is minimum when  $(x_j, y_j) = (x_i, y_i)$ . Therefore,  $\omega_j$  is always smaller than unity. The influence of the weight function will be studied in Section 4.4.

**Remark 5.** Boundary treatment. In the MSR, the technique of least-squares is used in every step. Therefore, it is necessary to ensure sufficient number of reconstruction relations on the boundary cells with at least one edge on the boundaries of the domain. It can be found in Fig. 3 that some cells e.g. corner cell  $\Omega_{corner}$  may not satisfy this requirement. For this reason, some special treatment is needed for the boundary cells. We denote that  $\Omega_i$  is a boundary cell usually with two internally neighboring control volumes  $\Omega_{j_k}$  ( $k = 1, 2$ ). For some special case e.g. Fig. 3, there is only one internally neighboring cell. To ensure there are always sufficient number of relations in the reconstruction algorithms, an asynchronous procedure is proposed. The idea of this procedure is in each step to perform the MSR for the internal cells first, then to use the resulting RRR on cells that are adjacent to the boundary cell (after applying the CT) as the reconstruction relations of the boundary cell of the same step. In Step 1, the proposed procedure is firstly applied on the internal cells to obtain the RRR of Eq. (51). Then on boundary cell  $\Omega_i$ , Eq. (51) of the internally face-neighboring cells  $\Omega_{j_k}$  ( $k = 1, 2$ ) is used as the reconstruction relations of cell  $\Omega_i$ , i.e.

$$\begin{bmatrix} A_{j_1,1}^+ A_{j_1} T_{j_1} \\ A_{j_2,1}^+ A_{j_2} T_{j_2} \end{bmatrix} \mathbf{C}_i = \begin{bmatrix} A_{j_1,1}^+ \boldsymbol{\alpha}_{j_1} \\ A_{j_2,1}^+ \boldsymbol{\alpha}_{j_2} \end{bmatrix},$$

which can be denoted as

$$A_i \mathbf{C}_i = \boldsymbol{\alpha}_i,$$

where  $A_i$  is a system with  $2 \times 2 = 4$  equations when the boundary cell has two neighboring internal cells (2 equations for case with only one neighboring internal cell). Therefore, it is sufficient to obtain the RRR of the first step for the boundary cell. In *Step 2*, the same procedure is used. At first, we implement *Step 2* on internal cells to obtain the RRR of Eq. (56). Then *Step 2* is implemented on boundary cell  $\Omega_i$  using the following reconstruction relations

$$\begin{bmatrix} A_{i,1}^+ A_i \\ B_{j_1,12}^+ B_{j_1} T_{j_1} \\ B_{j_2,12}^+ B_{j_2} T_{j_2} \end{bmatrix} \mathbf{C}_i = \begin{bmatrix} A_{i,1}^+ \boldsymbol{\alpha}_i \\ B_{j_1,12}^+ \boldsymbol{\beta}_{j_1} \\ B_{j_2,12}^+ \boldsymbol{\beta}_{j_2} \end{bmatrix}, \quad (59)$$

which can be denoted as

$$B_i \mathbf{C}_i = \boldsymbol{\beta}_i,$$

where the first line of Eq. (59) is the RRR of  $\Omega_i$  obtained in *Step 1*, the least two lines are the RRR obtained in *Step 2* for the internally adjacent cells.  $B_i$  is a system of  $2 + 5 \times 2 = 12$  equations ( $2 + 5 = 7$  equations for case with only one neighboring internal cell). Therefore, they are sufficient to obtain the RRR of *Step 2* for the boundary cells. The same procedure can be applied in *Step 3*. Although the above mentioned procedure can obtain the same degree reconstruction polynomials on the boundary cells as on the boundary cells, sometimes numerical instability will occur. It is found that when one-degree lower reconstruction polynomials are adopted on the boundary cells, the computation is stable. Therefore, in the present paper, the accuracy of the boundary cells is one order lower than that of the internal cells. The physical boundary conditions are applied directly in the numerical fluxes.

**Remark 6.** Extension to general polygonal cells. The extension of the MSR method to quadrangle cells or general polygonal cells is quite straightforward although only the triangular mesh case is presented in this paper. In each step, we collect the RRR of current and face neighboring cells to construct more relations to perform higher order accurate reconstructions. The crucial limit is the number of RRR that can be provided from face neighboring cells. It is apparent that quadrangle cells or general polygonal cells can provide more RRR than the triangular cells. Therefore, it is also feasible to perform MSR on non-triangular cells.

**Remark 7.** Comparing with the high order accurate k-exact reconstruction, the advantage of the present method is that the data structure of the present method is always based on the compact stencil. This feature makes it possible to design a code with different orders of accuracy without the need of constructing different data structures. This is especially important for the p-adaptation computation, which will be studied in a future paper. This feature is also beneficial in h-adaptation computation where a frequent searching of the reconstruction stencil is need. Comparing with the CLSFV [39] and VR [40] methods, the significant feature of the present method is that it can be used readily with both explicit and implicit time marching schemes. This is important in the simulation of very fast transient problems with the time scale being smaller than the time step determined by the CFL condition. In this case, the use of implicit time marching scheme is not advantageous. The implicit nature of the CLSFV and VR will adversely affect the efficiency of the schemes.

### 3.3. High order accurate finite volume schemes in terms of multi-step reconstruction

#### Governing equations

In this section, 2D Euler equations are presented as the governing equations

$$\frac{\partial \mathbf{U}}{\partial t} + \frac{\partial \mathbf{F}}{\partial x} + \frac{\partial \mathbf{G}}{\partial y} = 0. \quad (60)$$

The conservative variables  $\mathbf{U}$  and the inviscid flux  $\mathbf{F}, \mathbf{G}$  are given by

$$\mathbf{U} = \begin{bmatrix} \rho \\ \rho u \\ \rho v \\ \rho E \end{bmatrix}, \quad \mathbf{F} = \begin{bmatrix} \rho u \\ \rho u^2 + p \\ \rho uv \\ \rho uH \end{bmatrix}, \quad \mathbf{G} = \begin{bmatrix} \rho v \\ \rho uv \\ \rho v^2 + p \\ \rho vH \end{bmatrix}. \quad (61)$$

In Eq. (61)  $\rho$  represents the density,  $p$  represents the pressure,  $u$  and  $v$  represent the x- and y-velocity component respectively,  $E$  and  $H$  represent the specific total energy and the specific total enthalpy respectively, where  $E = \frac{1}{\gamma-1} \frac{p}{\rho} + \frac{1}{2}(u^2 + v^2)$ ,  $H = E + \frac{p}{\rho}$ .

In finite volume method, we first integrate Eq. (60) on the control volume e.g. element  $\Omega_i$

$$\frac{\partial}{\partial t} \int_{\Omega_i} \mathbf{U} d\Omega + \int_{\Omega_i} \nabla \cdot \Phi d\Omega = 0, \quad (62)$$



where  $\Phi = [\mathbf{F}, \mathbf{G}]$ . The application of Gauss theorem to Eq. (62) yields

$$\frac{\partial}{\partial t} \int_{\Omega_i} \mathbf{U} d\Omega + \sum_{m=1}^3 \int_{l_m} \Phi \cdot \mathbf{n} dl = 0.$$

The introduction of the cell average of  $\mathbf{U}$  defined similar to Eq. (43) leads to

$$\frac{\partial \bar{\mathbf{U}}_i}{\partial t} + \frac{1}{|\Omega_i|} \sum_{m=1}^3 \int_{l_m} \Phi \cdot \mathbf{n} dl = 0.$$

For high order FVS, integral on each side can be approximated with Gaussian quadrature:

$$\frac{\partial \bar{\mathbf{U}}_i}{\partial t} + \frac{1}{|\Omega_i|} \sum_{m=1}^3 \left( l_m \sum_{ng=1}^{NG} w_{ng} \Phi(\mathbf{U}_{ng}) \cdot \mathbf{n}_m \right) = 0, \quad (63)$$

where  $NG$  is the number of Gaussian points and  $NG_m = 2$  for a 4th order accurate FV schemes.

#### Curved boundary

The accuracy of high order schemes degrades with the general straight segments approximation of curved boundaries used in second order schemes [4]. The method of [45] is implemented to treat curved boundaries in this paper. In Section 4.5, a comparison for the numerical results with and without curved boundary treatment is presented.

#### Limiter

The discontinuities of the solution lead to non-physical oscillations in the reconstruction procedure. In this paper, the WBAP-L2 limiter [46,47] based on the secondary reconstruction [48] is used for capturing the discontinuities, that is

$$W = W^{L2}(1, \theta_1, \dots, \theta_J) = \frac{n_P + \sum_{k=1}^J 1/\theta_k^{p-1}}{n_P + \sum_{k=1}^J 1/\theta_k^p},$$

where parameters are set as  $p = 4$ ,  $n_P = 10$ . To improve the efficiency, a problem-independent shock detector [48] is used to determine the “trouble cells” where the WBAP limiter is used. The smoothness indicator  $IS_i$  is defined as

$$IS_i = \frac{\sum_{j \in S_i} |u_i(\mathbf{x}_i) - u_j(\mathbf{x}_i)|}{N_i h_i^{(k+1)/2} \max(\bar{u}_j, \bar{u}_i)},$$

where  $N_i$  is the number of face-neighbor cells thus  $N_i = 3$  for triangular cells. The shock detector is based on the utilization of the smoothness indicator:

$$(IS_i < \bar{S}_{dis}) = \begin{cases} True & \text{smooth region} \\ False & \text{shock region} \end{cases}.$$

In this paper,  $\bar{S}_{dis}$  is chosen to be 1 for MSR scheme and this parameter works well for numerical tests presented.

#### Numerical flux

The reconstruction procedure provides the cellwise approximation of  $\mathbf{U}$  to the flux function  $\Phi(\mathbf{U}_{ng})$  in Eq. (63). The flux can be evaluated with the flux splitting procedures, i.e.

$$\Phi(\mathbf{U}_{ng}) \cdot \mathbf{n}_m = \hat{\Phi}(\mathbf{U}^L(\mathbf{x}_{ng}), \mathbf{U}^R(\mathbf{x}_{ng}), \mathbf{n}_m).$$

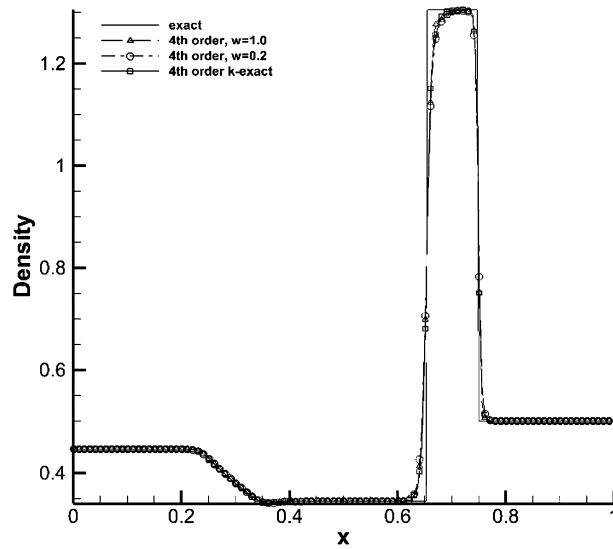
The standard Roe Riemann solver [49] with the entropy fix of Harten [50] is used in this paper.

#### Temporal discretization

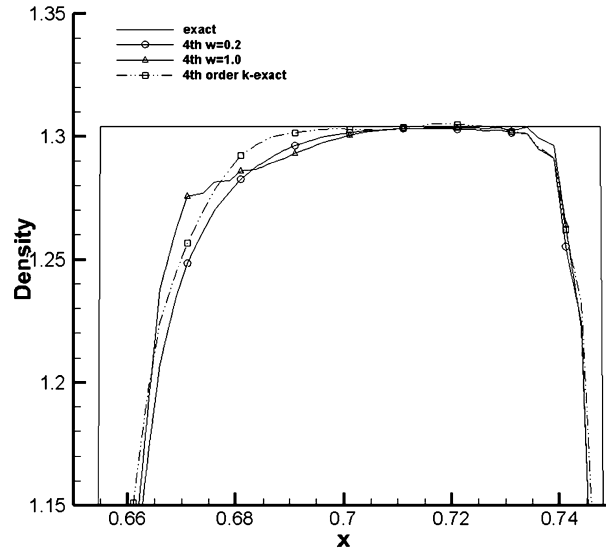
After calculation of numerical fluxes, Eq. (63) becomes a system of ODEs with respect to the time variable  $t$ . In this paper, a three stage TVD Runge-Kutta scheme [28] is implemented in as in the 1-D case.

## 4. Numerical results

Numerical tests are presented in this section. These tests demonstrate the property of MSR scheme on 1-D and 2-D unstructured grids. 1-D tests are presented in Sections 4.1–4.3; 2-D tests are presented in Sections 4.4–4.8.



(a) Entire view



(b) Enlargements

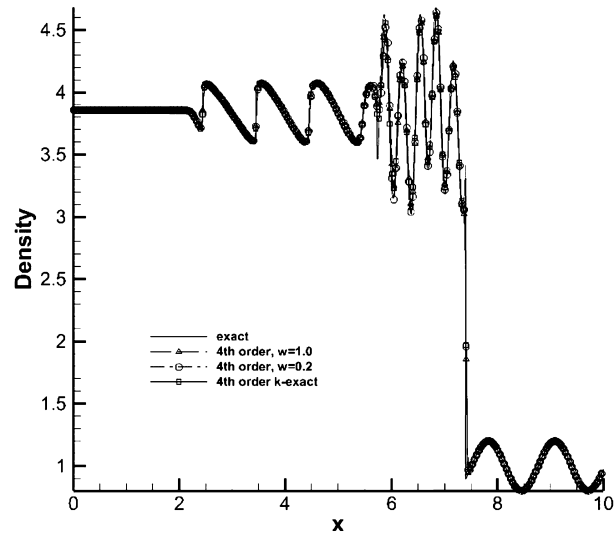
Fig. 4. Lax problem. Density distribution at  $t = 0.1$ .

#### 4.1. Lax problem [55]

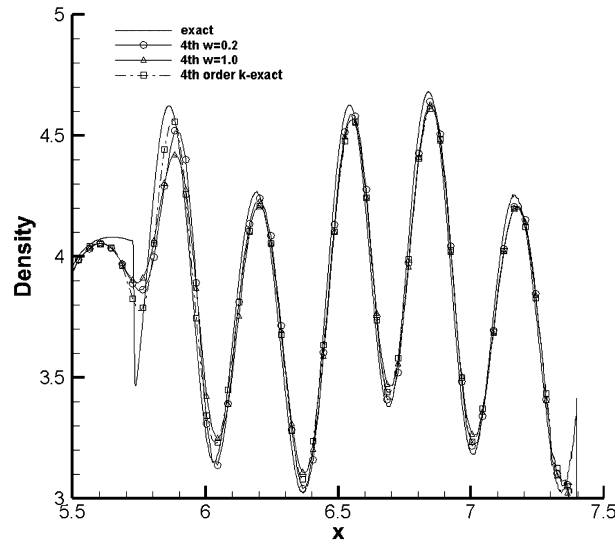
This test is a well-known shock tube problem. The initial conditions are

$$(\rho_0, u_0, p_0) = \begin{cases} (0.445, 0.698, 3.528) & \text{for } 0 \leq x \leq 0.5 \\ (0.5, 0, 0.571) & \text{otherwise} \end{cases} \quad (0 \leq x \leq 1).$$

In this test, 4th order accurate MSP schemes with WBAP limiter are implemented. The computation domain contains 200 cells and the results are presented until  $t = 0.1$ . The density distribution of results is shown in Fig. 4. Solutions of these schemes show good resolution. The Lax problem is a tough test case for non-characteristic-based schemes according to [30] that oscillations can easily appear for such schemes. On the other hand, the multi-step schemes demonstrate good shock capturing capability.



(a) Entire view



(b) Enlargements

**Fig. 5.** Shu-Osher problem. Density distribution at  $t = 1.8$ .

#### 4.2. Shu-Osher problem

This test is another well-known problem which describes the interaction of an entropy sine wave with a Mach 3 right moving shock. The initial conditions are

$$(\rho_0, u_0, p_0) = \begin{cases} (3.857143, 2.629369, 10.33333) & \text{for } 0 \leq x \leq 0.5 \\ (1 + 0.2 \sin(5x), 0, 1) & \text{otherwise} \end{cases} \quad (0 \leq x \leq 10)$$

In this test, 4th order accurate MSR schemes with WBAP limiter are implemented. The computation domain contains 500 cells and the results are presented until  $t = 1.8$ . The density distribution of results is shown in Fig. 5. Numerical solution of the 5th order WENO scheme [29] using 20000 cells is used as the exact solution. These results also demonstrate high resolution of the scheme. In terms of numerical dissipation, the present multi-step scheme is slightly larger than the k-exact FV scheme. When using a smaller weight ( $\omega = 0.2$ ), the numerical dissipation is also smaller than the case using  $\omega = 1$ . This result is in accordance with the Fourier analysis.

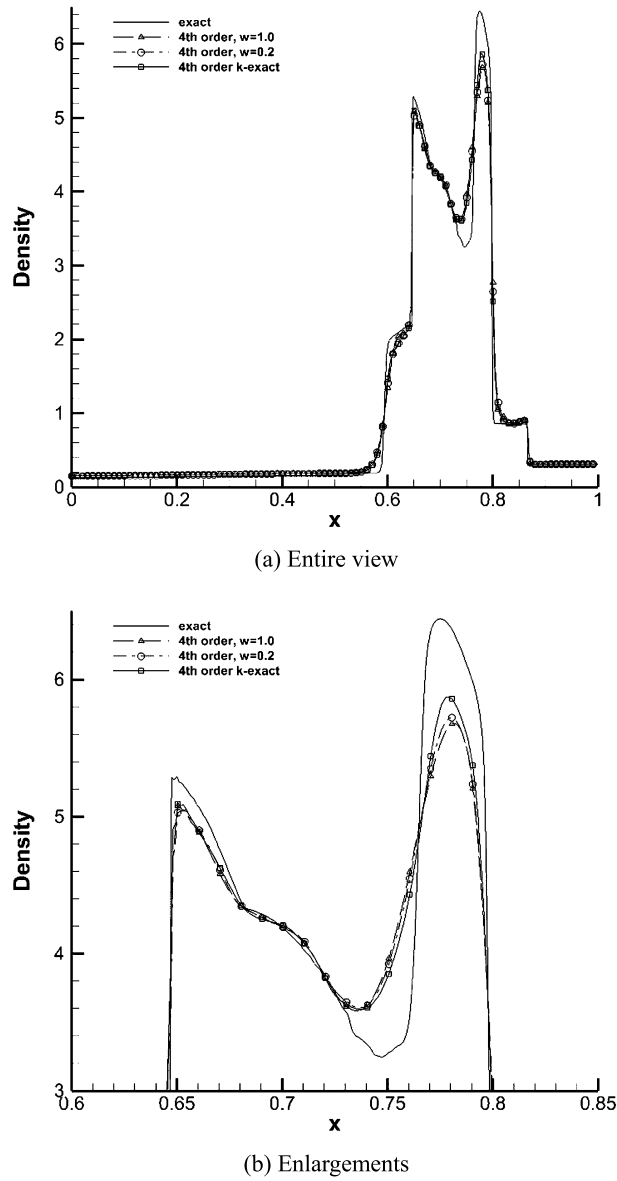


**Fig. 6.** Two interacting waves. Density distribution at  $t = 0.038$ .

#### 4.3. Two interacting blast wave test [54]

Simulation of the interaction of two blast waves is presented in this test. The computational domain is  $[0, 1]$  with 400 cells. Reflective boundary conditions are imposed at  $x = 0$  and  $x = 1$ . The initial condition is

$$(\rho, u, p) = \begin{cases} (1, 0, 1000) & \text{for } 0 \leq x \leq 0.1 \\ (1, 0, 0.01) & \text{for } 0.1 \leq x \leq 0.6 \\ (1, 0, 100) & \text{otherwise} \end{cases}.$$

The problem is solved using the 4th order accurate MSR scheme. The Courant number is  $CFL = 1.0$ . Density profiles at  $t = 0.038$  s are presented in Fig. 6. In this test, the result of 5th order WENO scheme with 2000 cells is treated as the exact solution. The result of scheme with  $\omega = 0.2$  is slightly better compared to scheme with  $\omega = 1.0$ .

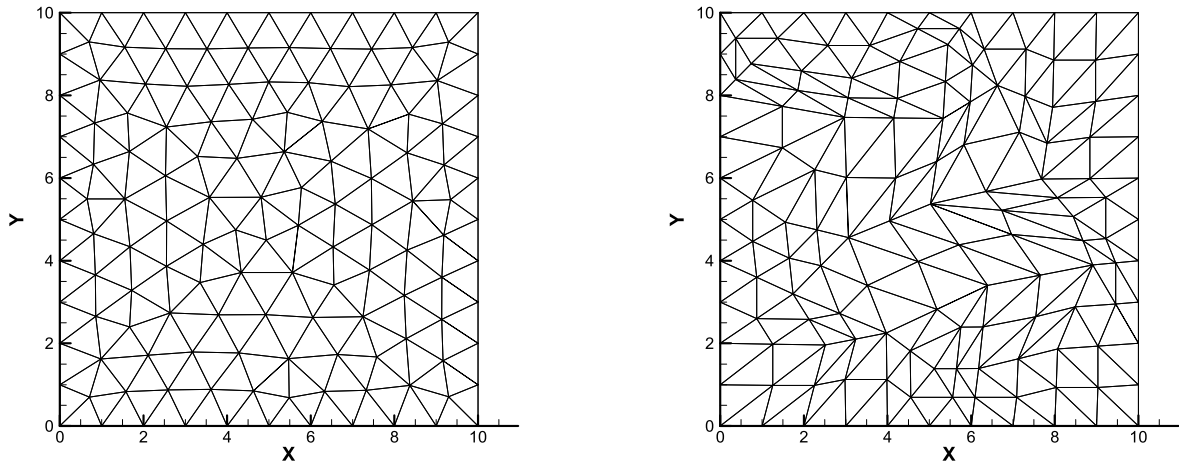


Fig. 7. Regular and irregular grids for the isentropic vortex problem with size  $h = 1$ .

Table 1

Accuracy tests for the isentropic vortex problem on regular grids.

Schemes	Grid size	L1 error	Order	L $\infty$ error	Order
4th order MSR	1	3.69E-03		4.41E-02	
	1/2	4.86E-04	2.92	1.09E-02	2.02
	1/4	2.72E-05	4.16	5.96E-04	4.20
	1/8	1.22E-06	4.48	3.08E-05	4.27
	1/16	7.22E-08	4.08	1.68E-06	4.20
4th order k-exact	1	4.41E-03		4.63E-02	
	1/2	4.20E-04	3.39	1.05E-02	2.14
	1/4	2.66E-05	3.98	5.30E-04	4.31
	1/8	1.21E-06	4.45	3.23E-05	4.04
	1/16	7.11E-08	4.09	1.69E-06	4.26
3rd order MSR	1	8.17E-03		1.22E-01	
	1/2	1.71E-03	2.26	3.13E-02	1.96
	1/4	2.89E-04	2.57	5.57E-03	2.49
	1/8	3.84E-05	2.91	7.67E-04	2.86
	1/16	4.77E-06	3.01	1.02E-04	2.91

#### 4.4. Isentropic vortex problem

This test is chosen to assess the accuracy of MSR scheme for computing the 2-D inviscid isentropic vortex problem. The mean flow density  $\rho_\infty$ , velocity  $u_\infty$  and  $v_\infty$ , and pressure  $p_\infty$  are given as  $(\rho_\infty, u_\infty, v_\infty, p_\infty) = (1, 1, 1, 1)$ . And the computational domain is  $[0, 10] \times [0, 10]$  with periodic boundaries in two directions.

An isentropic vortex is added to the mean flow field as an initial condition. The following perturbation values are given by

$$(\delta u, \delta v) = \frac{\chi}{2\pi} e^{0.5(1-r^2)} (-\bar{y}, \bar{x}),$$

$$\delta T = -\frac{(\gamma - 1)\chi^2}{8\gamma\pi^2} e^{1-r^2},$$

$$\delta(S = p/\rho^\gamma) = 0,$$

where  $(\bar{x}, \bar{y}) = (x - 5, y - 5)$ ,  $r^2 = \bar{x}^2 + \bar{y}^2$ ,  $\gamma = 1.4$  and  $\chi$  is the vortex strength. Here  $\chi = 5$  and  $T = \frac{p}{\rho}$ . The results are presented at  $t = 2.0$ . There are 2 types of grids used in the numerical computation, namely regular and irregular grids as shown in Fig. 7.

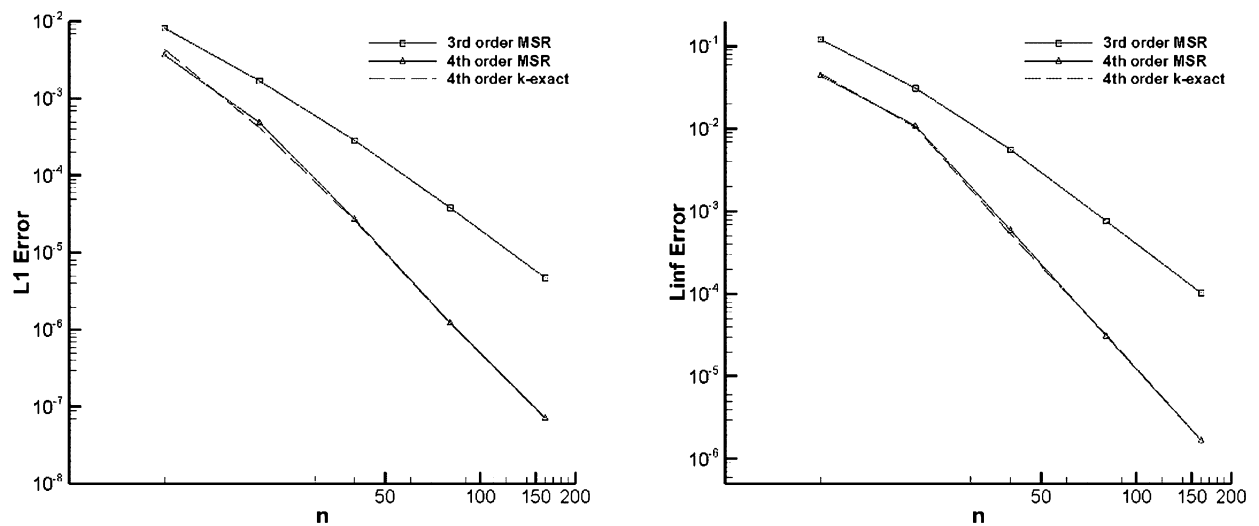
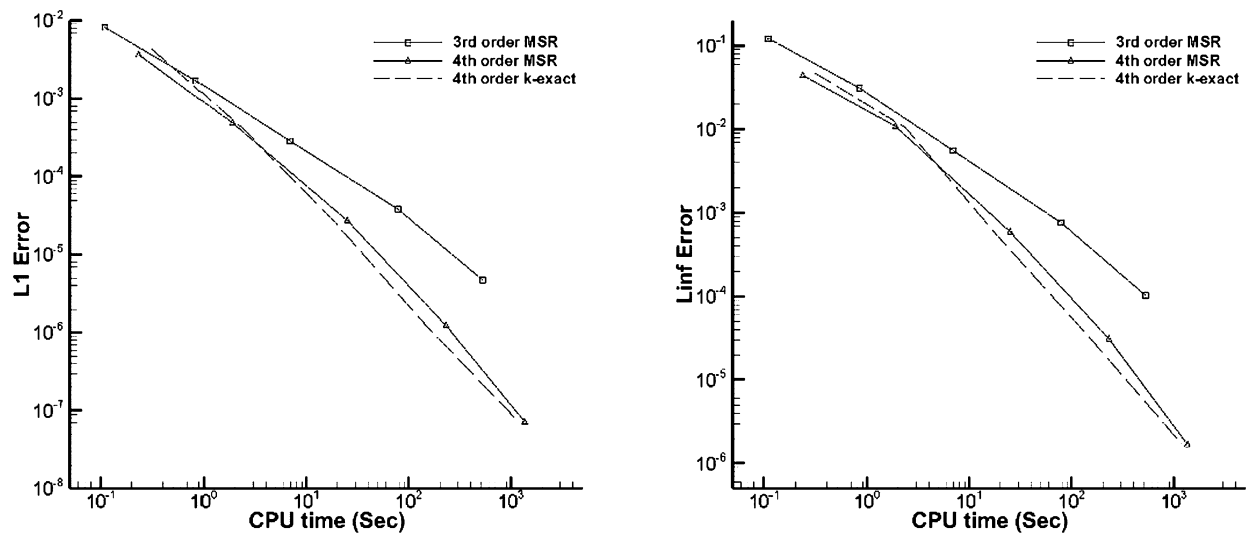
The grid sizes are chosen to be 1 to 1/16. The CFL number is chosen to be 1. The exact solution is a convection of the vortex with the mean flow and thus the accuracy can be easily calculated. In this test, accuracy of 3rd and 4th order MSR schemes on regular grids are presented in Table 1 compared with corresponding order k-exact schemes. Tests on irregular grids are presented in Table 2. The four-stage Runge-Kutta method [28] is used to reduce the influence of time discretization.

In Tables 1 and 2, the numerical accuracy of MSR scheme is demonstrated to reach the theoretical accuracy and is very close to that of the k-exact scheme. The accuracy and the efficiency comparison are shown in Fig. 8 and Fig. 9, respectively.

**Table 2**

Accuracy tests for the isentropic vortex problem on irregular grids.

Schemes	Grid size	L1 error	Order	$L_\infty$ error	Order
4th order MSR	1	1.01E-02		1.68E-01	
	1/2	2.29E-03	2.14	4.57E-02	1.88
	1/4	2.71E-04	3.08	6.12E-03	2.90
	1/8	2.06E-05	3.72	5.02E-04	3.61
	1/16	1.39E-06	3.89	3.31E-05	3.92
4th order k-exact	1	1.03E-02		1.59E-01	
	1/2	2.07E-03	2.31	3.74E-02	2.08
	1/4	2.16E-04	3.26	3.51E-03	3.41
	1/8	1.19E-05	4.18	2.35E-04	3.90
	1/16	5.59E-07	4.42	1.16E-05	4.34
3rd order MSR	1	1.27E-02		1.91E-01	
	1/2	4.99E-03	1.35	8.43E-02	1.18
	1/4	1.18E-03	2.08	2.28E-02	1.89
	1/8	2.02E-04	2.55	3.86E-03	2.56
	1/16	2.78E-05	2.86	5.50E-04	2.81

**Fig. 8.** Accuracy comparison for the isentropic vortex problem on regular grids.**Fig. 9.** Efficiency comparison for the isentropic vortex problem on regular grids.

**Table 3**

$L_1$  errors of the weighted MSR scheme for the isentropic vortex problem on regular and irregular grids with size of 1/16. Compare to the result 7.23E-08 and 1.39E-06 in Table 1 and Table 2 respectively.

4th order weighted MSR	$\beta = 0.5$	$\beta = 1.0$	$\beta = 1.5$	$\beta = 2.0$
Regular grids	6.80E-08	6.46E-08	6.23E-08	6.12E-08
Irregular grids	1.32E-06	1.22E-06	1.09E-06	9.62E-07

In Fig. 9, the efficiency of MSR scheme in terms of the numerical errors at the same CPU time is also compared with the k-exact scheme. The efficiency of the present scheme is also very close to the k-exact scheme. Specifically, it is shown that when the grids are coarse, the efficiency of the MSR scheme is slightly higher than that of the k-exact scheme. When the grids are finer, the MSR scheme is slightly lower in efficiency than the k-exact scheme. This is not surprising since the computational cost of the final step of the MSR is similar to that of the k-exact reconstruction. The previous steps of the MSR need only to solve systems of linear equations with considerably smaller size, and thus the computational cost is very small comparing with the last step.

There is another test for the purpose to verify the effect of the weights on the 4th order MSR scheme as shown in Remark 4 of Section 3. In Table 3,  $L_1$  errors on regular and irregular grids with grid size of 1/16 using different  $\beta$  in the weights are shown. With the increase of  $\beta$ , the reduction of errors can be observed. However, the errors are not very sensitive to the choice of the weight function. For simplicity, in other test cases, we still use the original MSR schemes without using the weights.

#### 4.5. Subsonic flows past a circular cylinder

This test is chosen to assess the accuracy of the MSR scheme with boundary treatments for the subsonic flow past a circular cylinder at a Mach number of  $M_\infty = 0.38$  [53]. The problem is calculated with curved boundaries. The five successively refined O-type grids used in this test are shown in Fig. 10, which consist of  $16 \times 9$ ,  $32 \times 17$ ,  $64 \times 33$ ,  $128 \times 65$  and  $256 \times 129$  grid points, respectively. The first number refers to the number of points in the circumferential direction, and the second refers to the number of concentric circles in the mesh. The radius of the cylinder is  $r_1 = 0.5$ , the domain is bounded by  $r_{129} = 40$ , and the radii of concentric circles for  $256 \times 129$  mesh are set up as

$$r_i = r_1 \left( 1 + \frac{2\pi}{256} \sum_{j=1}^{i-1} \alpha^j \right), \quad i = 2, \dots, 129,$$

where  $\alpha = 1.03803945$ . The coarser grids are generated by successively un-refining the finest mesh.

The CFL number used in temporal discretization is 1. To measure the order of accuracy, we used the following entropy production  $\varepsilon$  defined by

$$\varepsilon \doteq \frac{p}{p_\infty} \left( \frac{\rho_\infty}{\rho} \right)^\gamma - 1 \quad (64)$$

as the error measurement. The results of 3rd and 4th order MSR scheme described in Section 3 are listed in Table 4. The results demonstrate that the expected order of accuracy can be achieved even if one lower order reconstruction is implemented at the boundary cells as described in Remark 5 of Section 3.

In Table 5, there is a comparison between the numerical results using curved control volumes near the boundary and treating boundary as segments of straight lines. It is shown that using straight-edge cells in high order schemes will significantly increase the numerical error and reduce the order of accuracy.

**Table 4**

Accuracy tests for the subsonic flow past a circular cylinder problem.

Schemes	Grid size	L1 error	Order	L2 error	Order
4th order MSR	$16 \times 9$	1.61E-02		3.78E-02	
	$32 \times 17$	1.69E-03	3.25	6.34E-03	2.58
	$64 \times 33$	1.08E-04	3.97	6.10E-04	3.38
	$128 \times 65$	6.84E-06	3.98	5.42E-05	3.49
	$256 \times 129$	4.64E-07	3.88	4.87E-06	3.48
3rd order MSR	$16 \times 9$	1.30E-02		3.05E-02	
	$32 \times 17$	2.44E-03	2.41	7.52E-03	2.02
	$64 \times 33$	3.15E-04	2.95	1.16E-03	2.69
	$128 \times 65$	3.89E-05	3.02	1.74E-04	2.74
	$256 \times 129$	4.86E-06	3.00	2.75E-05	2.66

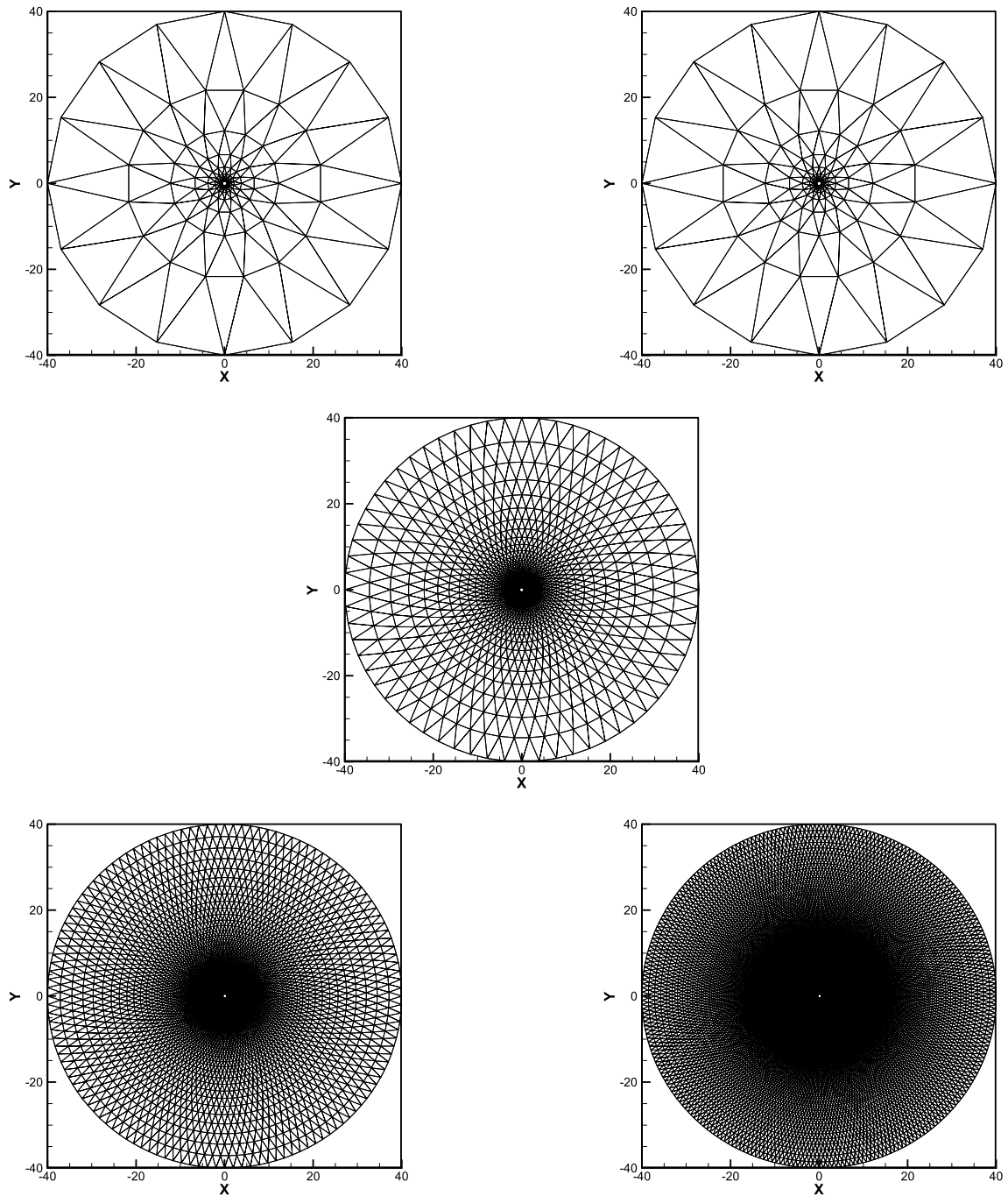


**Fig. 10.** Sequences of five successively globally refined meshes for the subsonic flow past a circular cylinder problem.

#### 4.6. Subsonic flow around NACA0012 airfoil

This test is chosen to verify the convergence of the MSR schemes in a steady flow simulation. The mesh used in the test is presented in Fig. 11, consisting of 10382 elements, 5306 grid points and 150 boundary points. The problem is calculated by considering the effect of the curved boundaries.

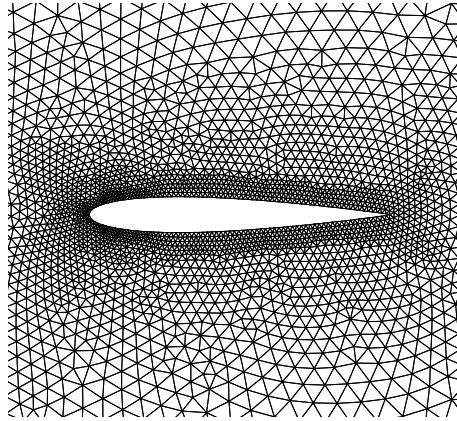
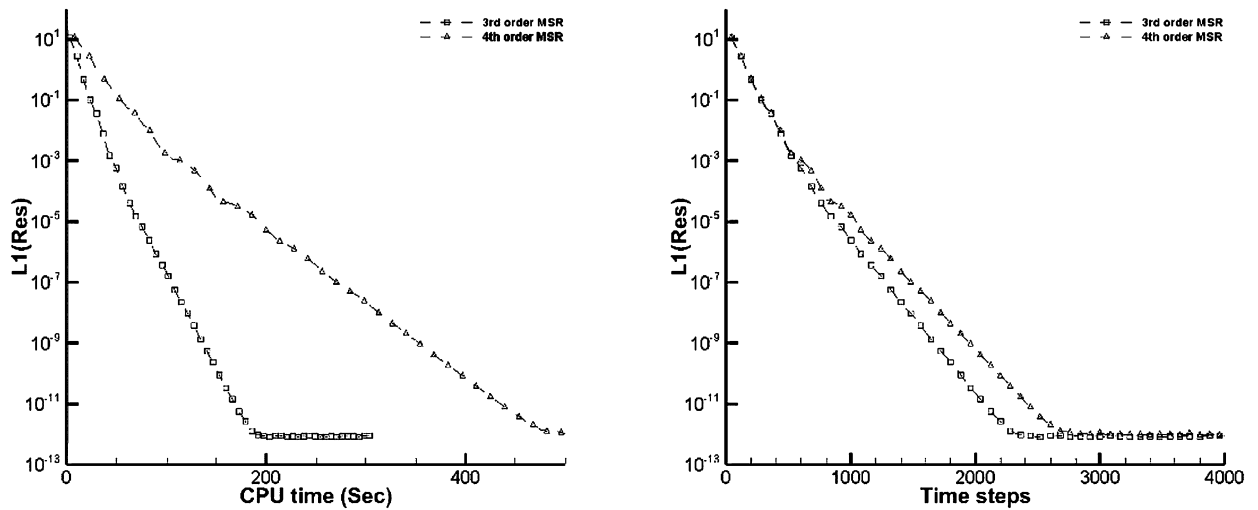
The far field flow is the Mach 0.3 subsonic inflow at the angle of attack of  $2^\circ$ . In this test, results of 3rd and 4th order MSR schemes are presented. The implicit Runge-Kutta method is used for the improvement of convergence [39]. The CFL number is 40. Results are presented in Figs. 12 and 13. The former demonstrates the convergence history of the residual of density. The latter demonstrates the accuracy based on the entropy error defined in Eq. (64). As shown in Fig. 12, good



**Table 5**

Comparison between curved and straight line boundary approximation.

Schemes	Grid size	L1 error	Order	L2 error	Order
4th order MSR with curved boundary	$16 \times 9$	1.61E-02		3.78E-02	
	$32 \times 17$	1.69E-03	3.25	6.34E-03	2.58
	$64 \times 33$	1.08E-04	3.97	6.10E-04	3.38
	$128 \times 65$	6.84E-06	3.98	5.42E-05	3.49
	$256 \times 129$	4.64E-07	3.88	4.87E-06	3.48
4th order MSR without curved boundary	$16 \times 9$	1.70E-02		4.09E-02	
	$32 \times 17$	1.75E-03	3.28	7.18E-03	2.51
	$64 \times 33$	1.93E-04	3.18	1.04E-03	2.79
	$128 \times 65$	3.53E-05	2.45	2.64E-04	1.98
	$256 \times 129$	8.04E-06	2.13	8.93E-05	1.56

**Fig. 11.** Mesh for the subsonic flow around NACA0012 airfoil problem.**Fig. 12.** Convergence history comparison for subsonic flow around NACA0012 airfoil problem.

convergence can be achieved. And Fig. 13 indicates that the higher (4th) order MSR scheme is more accurate than the lower (3rd) order MSR scheme.

#### 4.7. Double Mach reflection of a strong shock wave

The double Mach reflection test [54] is a well-known case that is calculated with high-resolution. The computational domain is  $[0, 4] \times [0, 1]$ . An incident right moving  $M_t = 10$  shock is initially located at  $(1/6, 0)$ , inclined  $60^\circ$  with respect to the x-axis. The results are presented at  $t = 0.2$ .

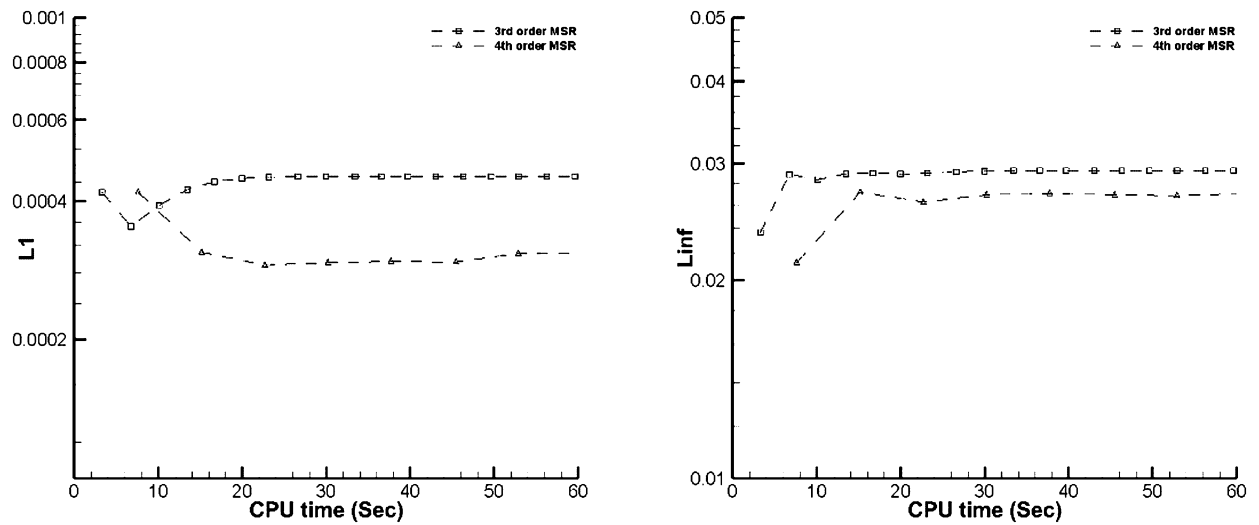


Fig. 13. Entropy error comparison for subsonic flow around NACA0012 airfoil problem.

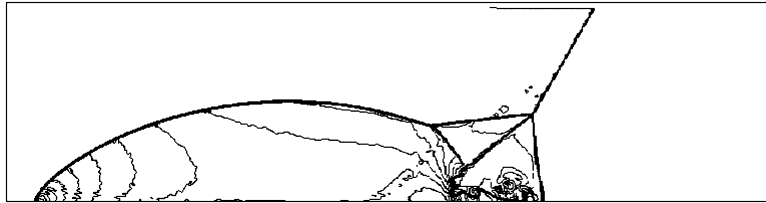


Fig. 14. Density contours for double Mach reflection on grids with size  $h = 1/240$ . Thirty equally spaced contour lines between 2.05 and 21.31.

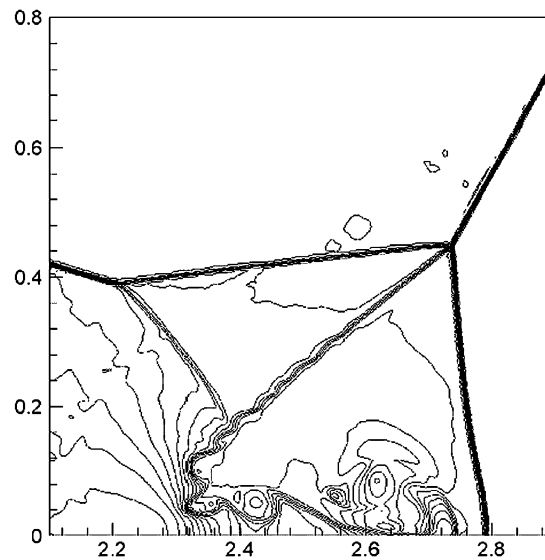


Fig. 15. Close-up view around the double Mach stem of Fig. 14.

The mesh size in this test is  $1/240$  and the CFL number is 1. The WBAP limiter presented in Section 3 is used in computations. In this test, numerical solutions of 4th order MSR scheme is presented with the density contours shown in Fig. 14 and Fig. 15. It is clear that the solutions are oscillation-free and schemes are robust enough to capture the complicated flow structures in high resolution.

#### 4.8. The Sedov blast wave problem

We calculate the 2D Sedov blast wave problem [58] to verify the robustness of the limiter and shock detector. An exact solution is available in [59]. The computational domain is  $[0, 1.2] \times [0, 1.2]$ . The grid size is chosen to be 0.02 thus the mesh has 60 grids in one dimension. The initial condition is set to be

$$\begin{cases} \rho_0 = 1 \\ u_0 = 0 \\ v_0 = 0 \\ p_0 = 0, \text{ except at the origin} \end{cases}.$$

An initial delta-function energy source is set at the origin and the initial pressure in the cell containing origin is  $p_{or} = (\gamma - 1)\rho_{or}\frac{\varepsilon_0}{V_{or}}$ , where  $\gamma = 1.4$ ,  $V_{or}$  denotes the volume of the cell containing origin and  $\varepsilon_0$  is the total amount of release energy. In this paper, we choose  $\varepsilon_0 = 0.244816$  as suggested in [58,59]. This initial amount of energy is chosen to locate the front of the shock wave at radius  $r = 1$  at  $t = 1$ . Since vacuum cannot be simulated, we set the initial pressure to be  $10^{-6}$  over the computational domain except at the origin.

It is found that larger dissipation of the limiter is required to guarantee the stability of the computation. In this test case, we chose the weight of center cell in WBAP limiter to be 1, compared to 10 in other test cases in this paper.

In this test, we present results from the 4th-order MSR method. The density and the pressure profiles are performed in Fig. 16. The robustness of the limiter and shock detector is verified.

### 5. Conclusion

In this paper, MSR procedure is presented for finite volume method on both 1D grids and 2D unstructured grids. MSR is a recursive algorithm which can eventually provide sufficient relations for high order reconstruction in a multi-step procedure. In each step, the PIT is used to regularize the existing reconstruction relations which are usually not sufficient to perform the high order reconstruction but are sufficient to obtain the RRR of the next step. And in the next step, the RRR on the face-neighboring cells after applying the CT and those on the current cell are utilized to construct new reconstruction relations which can be used to perform higher order reconstruction. In 1D case, the Fourier analysis is presented to study the dispersion/dissipation properties of the semi-discretized FV schemes based on the MSR for solving the scalar linear advection equation. In 2D case, the application of the MSR in high order accurate FV schemes solving 2D Euler equations are presented in detail. Several numerical tests are solved to show the properties of MSR schemes. The advantage of the present schemes is that they can achieve arbitrarily high order of accuracy on compact stencil.

### Acknowledgements

This work is supported by the National Natural Science Foundation of China (Grant No. 91752114 and 11672160). The 2D finite volume method framework is based on Qian Wang's code.

### Appendix A

In this appendix, the CT for the 1D and 2D cases are presented in detail. To ensure that the CT preserves the k-exactness of the reconstruction, the CT is derived assuming the exact solution is a cubic polynomial.

#### 1D case

We assume that  $u(x)$  is in the form of

$$u(x) = u_i + u'_i(x - x_i) + \frac{1}{2!}u''_i(x - x_i)^2 + \frac{1}{3!}u'''_i(x - x_i)^3 \quad (\text{A.1})$$

where subscript  $i$  denotes value at point  $x_i$ . In MSR,  $u$  is approximated as

$$u_i(x) = \bar{u}_i + \sum_{l=1}^3 C_i^{(l)} \phi_{l,i}(x) \quad (\text{A.2})$$

where  $\phi_{l,i}(x)$  is the zero-mean basis defined in Eq. (7). It is trivial to show that Eq. (A.1) and Eq. (A.2) are equivalent within  $\Omega_i$  if the following conditions are satisfied, which are

$$\begin{bmatrix} u_i^{(1)} \\ u_i^{(2)} \\ u_i^{(3)} \end{bmatrix} = \begin{bmatrix} 1/h_i & 0 & 0 \\ 0 & 2!/h_i^2 & 0 \\ 0 & 0 & 3!/h_i^3 \end{bmatrix} \begin{bmatrix} C_i^{(1)} \\ C_i^{(2)} \\ C_i^{(3)} \end{bmatrix} \quad (\text{A.3})$$

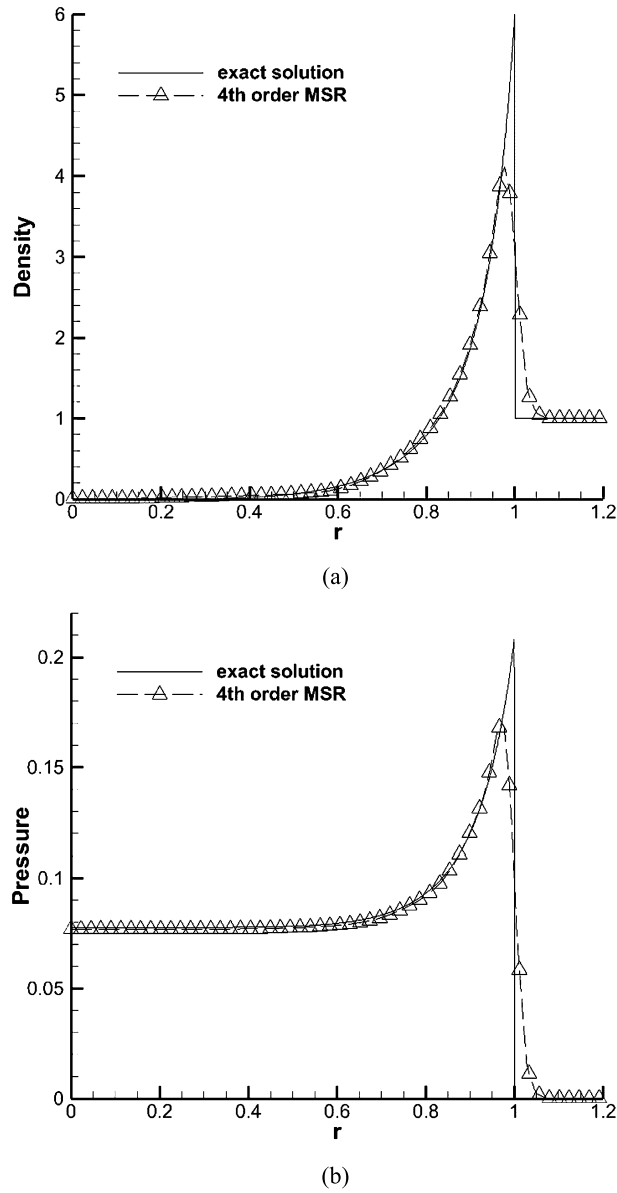


Fig. 16. Sedov blast wave problem. (a) Density and (b) pressure profiles at  $t = 1.0$ .

and

$$\langle u(x) \rangle^i = \bar{u}_i, \quad (\text{A.4})$$

where  $u_i^{(l)}$  is the  $l$ -th derivative of  $u(x)$ . Since Eq. (A.4) is the prerequisite condition for the FV scheme, Eq. (A.3) is satisfied exactly if  $u(x)$  is a cubic polynomial. This condition is also the basis of CT. Eq. (A.3) can be denoted as

$$\mathbf{u}_i^D = R_i \mathbf{C}_i \quad (\text{A.5})$$

Taylor expansions of  $u_j^{(l)}$  at  $x_i$  gives

$$\begin{cases} u_j^{(1)} = u_i^{(1)} + u_i^{(2)}(x_j - x_i) + \frac{1}{2!}u_i^{(3)}(x)(x_j - x_i)^2 \\ u_j^{(2)} = u_i^{(2)} + u_i^{(3)}(x_j - x_i) \\ u_j^{(3)} = u_i^{(3)} \end{cases}$$



## Appendix B

In this appendix, we will show that the proposed 1D 4th order accurate MSR method can recover a cubic polynomial exactly.

At first we suppose the cell average values is calculated using a cubic polynomial. For the sake of simplicity, we choose polynomial basis functions to be  $\phi_{1,i}, \phi_{2,i}, \phi_{3,i}$  in cell  $i$ . The derivative vector is supposed to be  $\mathbf{C}_i^P$ . Thus, the form of the supposed cubic polynomial in cell  $i$  is

$$u_i(x) = \bar{u}_i + [\phi_{1,i}, \phi_{2,i}, \phi_{3,i}] \mathbf{C}_i^P.$$

In the following we will prove that  $\mathbf{C}_i^P$  satisfies the algorithm of 4th order accurate MSR method.

In the algorithm of *Step 1*, since the cubic polynomial distribution is defined on the whole domain and do not change in different cells, the following equations always hold

$$A_i \mathbf{C}_i^P = \alpha_i \quad (\text{B.1})$$

for all  $\Omega_i$ . This is the fundamental reason to make the reconstruction k-exact since all other operations are either exact or being the linear mapping of Eq. (B.1). The RRR obtained in the first step is Eq. (25), which leads to

$$A_{i,1}^+ A_i \mathbf{C}_i^P = A_{i,1}^+ \alpha_i \quad (\text{B.2})$$

using Eq. (B.1).

In the algorithm of *Step 2*, the reconstruction relations are

$$\begin{bmatrix} A_{i,1}^+ A_i \mathbf{C}_i^P \\ A_{i-1,1}^+ A_{i-1} \mathbf{C}_{i-1}^P \\ A_{i+1,1}^+ A_{i+1} \mathbf{C}_{i+1}^P \end{bmatrix} = \begin{bmatrix} A_{i,1}^+ \alpha_i \\ A_{i-1,1}^+ \alpha_{i-1} \\ A_{i+1,1}^+ \alpha_{i+1} \end{bmatrix} \quad (\text{B.3})$$

It is noticed that we have proved in the Appendix A that CT is precise for cubic polynomial

$$\mathbf{C}_j^P = T_{j(\rightarrow i)} \mathbf{C}_i^P. \quad (\text{B.4})$$

Applying the CT to Eq. (B.3), we have

$$\begin{bmatrix} A_{i,1}^+ A_i \mathbf{C}_i^P \\ A_{i-1,1}^+ A_{i-1} \mathbf{C}_{i-1}^P \\ A_{i+1,1}^+ A_{i+1} \mathbf{C}_{i+1}^P \end{bmatrix} = \begin{bmatrix} A_{i,1}^+ A_i \\ A_{i-1,1}^+ A_{i-1} T_{i-1} \\ A_{i+1,1}^+ A_{i+1} T_{i+1} \end{bmatrix} \mathbf{C}_i^P = \begin{bmatrix} A_{i,1}^+ \alpha_i \\ A_{i-1,1}^+ \alpha_{i-1} \\ A_{i+1,1}^+ \alpha_{i+1} \end{bmatrix} \quad (\text{B.5})$$

i.e.

$$B_i \mathbf{C}_i^P = \beta_i. \quad (\text{B.6})$$

Then one can derive

$$B_{i,12}^+ B_i \mathbf{C}_i^P = B_{i,12}^+ \beta_i. \quad (\text{B.7})$$

In the algorithm of *Step 3*, Eq. (B.6) and CT lead to

$$\begin{bmatrix} B_{i,12}^+ B_i \mathbf{C}_i^P \\ B_{i-1,12}^+ B_{i-1} \mathbf{C}_{i-1}^P \\ B_{i+1,12}^+ B_{i+1} \mathbf{C}_{i+1}^P \end{bmatrix} = \begin{bmatrix} B_{i,12}^+ B_i \\ B_{i-1,12}^+ B_{i-1} T_{i-1} \\ B_{i+1,12}^+ B_{i+1} T_{i+1} \end{bmatrix} \mathbf{C}_i^P = \begin{bmatrix} B_{i,12}^+ \beta_i \\ B_{i-1,12}^+ \beta_{i-1} \\ B_{i+1,12}^+ \beta_{i+1} \end{bmatrix} \quad (\text{B.8})$$

or

$$M_i \mathbf{C}_i^P = \gamma_i, \quad (\text{B.9})$$

and the final equation can be derived as

$$\mathbf{C}_i^P = M_i^+ \gamma_i. \quad (\text{B.10})$$

In the aforementioned Eqs. (B.1) and (B.3), equality is established by the supposing cubic polynomial distribution. In other equations, equality is established whether by combining equations or by pre-multiplying a matrix to the former equation. Then  $\mathbf{C}_i^P$  satisfies the algorithm of MSR. For a well-posed least squares problem, the solution is always unique. Then we have proved that the solution of 4th MSR method is  $\mathbf{C}_i^P$ , which means the cubic polynomial is recovered exactly.

## References

- [1] Z.J. Wang, Y. Liu, G. May, A. Jameson, Spectral difference method for unstructured grids II: extension to the Euler equations, *J. Sci. Comput.* 32 (1) (2007) 45–71.
- [2] T.J. Barth, P.O. Frederickson, Higher order solution of the Euler equations on unstructured grids using quadratic reconstruction, *AIAA Pap.* 90 (1990) 0013.
- [3] M. Delanaye, Y. Liu, Quadratic reconstruction finite volume schemes on 3D arbitrary unstructured polyhedral grids, *AIAA Pap.* 9 (9) (1989) 3259.
- [4] C. Ollivier-Gooch, M. Van Altena, A high-order-accurate unstructured mesh finite-volume scheme for the advection-diffusion equation, *J. Comput. Phys.* 181 (2) (2002) 729–752.
- [5] C.F. Ollivier-Gooch, Quasi-ENO schemes for unstructured meshes based on unlimited data-dependent least-squares reconstruction, *J. Comput. Phys.* 133 (1) (1997) 6–17.
- [6] O. Friedrich, Weighted essentially non-oscillatory schemes for the interpolation of mean values on unstructured grids, *J. Comput. Phys.* 144 (1) (1998) 194–212.
- [7] M. Dumbser, M. Käser, Arbitrary high order non-oscillatory finite volume schemes on unstructured meshes for linear hyperbolic systems, *J. Comput. Phys.* 221 (2) (2007) 693–723.
- [8] M. Dumbser, M. Käser, V.A. Titarev, E.F. Toro, Quadrature-free non-oscillatory finite volume schemes on unstructured meshes for nonlinear hyperbolic systems, *J. Comput. Phys.* 226 (1) (2007) 204–243.
- [9] C. Hu, C.W. Shu, Weighted essentially non-oscillatory schemes on triangular meshes, *J. Comput. Phys.* 150 (1) (1999) 97–127.
- [10] W.H. Reed, T.R. Hill, *Triangular Mesh Methods for the Neutron Transport Equation*, Los Alamos Report LA-UR-73-479, 1973.
- [11] B. Cockburn, C.W. Shu, TVB Runge-Kutta local projection discontinuous Galerkin finite element method for conservation laws. II. General framework, *Math. Comput.* 52 (186) (1989) 411–435.
- [12] B. Cockburn, S.Y. Lin, C.W. Shu, TVB Runge-Kutta local projection discontinuous Galerkin finite element method for conservation laws III: one-dimensional systems, *J. Comput. Phys.* 84 (1) (1989) 90–113.
- [13] B. Cockburn, S. Hou, C.W. Shu, The Runge-Kutta local projection discontinuous Galerkin finite element method for conservation laws. IV. The multidimensional case, *Math. Comput.* 54 (190) (1990) 545–581.
- [14] B. Cockburn, C.W. Shu, Runge-Kutta discontinuous Galerkin methods for convection-dominated problems, *J. Sci. Comput.* 16 (3) (2001) 173–261.
- [15] Z.J. Wang, Spectral (finite) volume method for conservation laws on unstructured grids: basic formulation, *J. Comput. Phys.* 178 (1) (2002) 210–251.
- [16] Z.J. Wang, Y. Liu, Spectral (finite) volume method for conservation laws on unstructured grids: II. Extension to two-dimensional scalar equation, *J. Comput. Phys.* 179 (2) (2002) 665–697.
- [17] Z.J. Wang, Y. Liu, Spectral (finite) volume method for conservation laws on unstructured grids III: one dimensional systems and partition optimization, *J. Sci. Comput.* 20 (1) (2004) 137–157.
- [18] Z.J. Wang, L. Zhang, Y. Liu, Spectral (finite) volume method for conservation laws on unstructured grids IV: extension to two-dimensional systems, *J. Comput. Phys.* 194 (2) (2004) 716–741.
- [19] Y. Liu, M. Vinokur, Z.J. Wang, Spectral difference method for unstructured grids I: basic formulation, *J. Comput. Phys.* 216 (2) (2006) 780–801.
- [20] Z.J. Wang, Y. Liu, G. May, A. Jameson, Spectral difference method for unstructured grids II: extension to the Euler equations, *J. Sci. Comput.* 32 (1) (2007) 45–71.
- [21] G. May, A. Jameson, A spectral difference method for the Euler and Navier-Stokes equations on unstructured meshes, *AIAA Pap.* 304 (2006).
- [22] M. Dumbser, D.S. Balsara, E.F. Toro, C.D. Munz, A unified framework for the construction of one-step finite volume and discontinuous Galerkin schemes on unstructured meshes, *J. Comput. Phys.* 227 (18) (2008) 8209–8253.
- [23] M. Dumbser, Arbitrary high order PNPM schemes on unstructured meshes for the compressible Navier-Stokes equations, *Comput. Fluids* 39 (1) (2010) 60–76.
- [24] M. Dumbser, O. Zanotti, Very high order PNPM schemes on unstructured meshes for the resistive relativistic MHD equations, *J. Comput. Phys.* 228 (18) (2009) 6991–7006.
- [25] L. Zhang, W. Liu, L. He, X. Deng, H. Zhang, A class of hybrid DG/FV methods for conservation laws I: basic formulation and one-dimensional systems, *J. Comput. Phys.* 231 (4) (2012) 1081–1103.
- [26] L. Zhang, W. Liu, L. He, X. Deng, H. Zhang, A class of hybrid DG/FV methods for conservation laws II: two-dimensional cases, *J. Comput. Phys.* 231 (4) (2012) 1104–1120.
- [27] A. Harten, B. Engquist, S. Osher, S.R. Chakravarty, Uniformly high order accurate essentially non-oscillatory schemes III, *J. Comput. Phys.* 71 (2) (1987) 231–303.
- [28] C.W. Shu, S. Osher, Efficient implementation of essentially non-oscillatory shock-capturing schemes, *J. Comput. Phys.* 77 (2) (1988) 439–471.
- [29] C.W. Shu, S. Osher, Efficient implementation of essentially non-oscillatory shock-capturing schemes, II, *J. Comput. Phys.* 83 (1) (1989) 32–78.
- [30] G.S. Jiang, C.W. Shu, Efficient implementation of weighted ENO schemes, *J. Comput. Phys.* 126 (1) (1996) 202–228.
- [31] D.S. Balsara, C.W. Shu, Monotonicity preserving weighted essentially non-oscillatory schemes with increasingly high order of accuracy, *J. Comput. Phys.* 160 (2) (2000) 405–452.
- [32] A.K. Henrick, T.D. Aslam, J.M. Powers, Simulations of pulsating one-dimensional detonations with true fifth order accuracy, *J. Comput. Phys.* 213 (1) (2006) 311–329.
- [33] R. Borges, M. Carmona, B. Costa, W.S. Don, An improved weighted essentially non-oscillatory scheme for hyperbolic conservation laws, *J. Comput. Phys.* 227 (6) (2008) 3191–3211.
- [34] D.S. Balsara, T. Rumpf, M. Dumbser, C.D. Munz, Efficient high accuracy ADER-WENO schemes for hydrodynamics and divergence-free magnetohydrodynamics, *J. Comput. Phys.* 228 (7) (2009) 2480–2516.
- [35] D.S. Balsara, Divergence-free reconstruction of magnetic fields and WENO schemes for magnetohydrodynamics, *J. Comput. Phys.* 228 (14) (2009) 5040–5056.
- [36] R. Abgrall, On essentially non-oscillatory schemes on unstructured meshes: analysis and implementation, *J. Comput. Phys.* 114 (1) (1994) 45–58.
- [37] R. Abgrall, A. Larat, M. Ricchiuto, Construction of very high order residual distribution schemes for steady inviscid flow problems on hybrid unstructured meshes, *J. Comput. Phys.* 230 (11) (2011) 4103–4136.
- [38] Q. Wang, Y.X. Ren, W. Li, Compact high order finite volume method on unstructured grids I: basic formulations and one-dimensional schemes, *J. Comput. Phys.* 314 (2016) 863–882.
- [39] Q. Wang, Y.X. Ren, W. Li, Compact high order finite volume method on unstructured grids II: extension to two-dimensional Euler equations, *J. Comput. Phys.* 314 (2016) 883–904.
- [40] Q. Wang, Y.X. Ren, W. Li, Compact high order finite volume method on unstructured grids III: variational reconstruction, *J. Comput. Phys.* 337 (2017) 1–26.
- [41] H.Q. Yang, Z.J. Chen, A. Przekwas, J. Dudley, A high-order CFD method using successive differentiation, *J. Comput. Phys.* 281 (2015) 690–707.
- [42] Florian Haider, Bernard Courbet, Jean-Pierre Croisille, A high-order compact reconstruction for finite volume methods: the one-dimensional case, 2015, <https://hal.archives-ouvertes.fr/hal-01284635/document>.

- [43] M.P. Martín, E.M. Taylor, M. Wu, V.G. Weirs, A bandwidth-optimized WENO scheme for the effective direct numerical simulation of compressible turbulence, *J. Comput. Phys.* 220 (1) (2006) 270–289.
- [44] S.K. Lele, Compact finite difference schemes with spectral-like resolution, *J. Comput. Phys.* 103 (1) (1992) 16–42.
- [45] W. Li, Y.X. Ren, The multi-dimensional limiters for discontinuous Galerkin method on unstructured grids, *Comput. Fluids* 96 (2014) 368–376.
- [46] W. Li, Y.X. Ren, The multi-dimensional limiters for solving hyperbolic conservation laws on unstructured grids II: extension to high order finite volume schemes, *J. Comput. Phys.* 231 (11) (2012) 4053–4077.
- [47] W. Li, Y.X. Ren, G. Lei, H. Luo, The multi-dimensional limiters for solving hyperbolic conservation laws on unstructured grids, *J. Comput. Phys.* 230 (21) (2011) 7775–7795.
- [48] W. Li, Y.X. Ren, High-order k-exact WENO finite volume schemes for solving gas dynamic Euler equations on unstructured grids, *Int. J. Numer. Methods Fluids* 70 (6) (2012) 742–763.
- [49] P.L. Roe, Approximate Riemann solvers, parameter vectors, and difference schemes, *J. Comput. Phys.* 43 (2) (1981) 357–372.
- [50] A. Harten, J.M. Hyman, Self adjusting grid methods for one-dimensional hyperbolic conservation laws, *J. Comput. Phys.* 50 (1983) 235–269.
- [51] B. Courbet, C. Benoit, V. Couaillier, F. Haider, M.C. Le Pape, S. Péron, Space discretization methods, *AerospaceLab* (2) (2011) 1.
- [52] V. Chiravalle, N. Morgan, A 3D Lagrangian cell-centered hydrodynamic method with higher-order reconstructions for gas and solid dynamics, <https://doi.org/10.1016/j.camwa.2018.06.011>.
- [53] H. Luo, J.D. Baum, R. Löhner, A Hermite WENO-based limiter for discontinuous Galerkin method on unstructured grids, *J. Comput. Phys.* 225 (1) (2007) 686–713.
- [54] P. Woodward, P. Colella, The numerical simulation of two-dimensional fluid flow with strong shocks, *J. Comput. Phys.* 54 (1) (1984) 115–173.
- [55] P.D. Lax, Weak solutions of nonlinear hyperbolic equations and their numerical computation, *Commun. Pure Appl. Math.* 7 (1) (1954) 159–193.
- [56] F. Xiao, Unified formulation for compressible and incompressible flows by using multi integrated moments I: one-dimensional inviscid compressible flow, *J. Comput. Phys.* 195 (2004) 629.
- [57] F. Xiao, R. Akoh, S. Li, Unified formulation for compressible and incompressible flows by using multi-integrated moments II: multidimensional version for compressible and incompressible flows, *J. Comput. Phys.* 213 (1) (2006) 31–56.
- [58] F. Vilar, C.W. Shu, P.H. Maire, Positivity preserving cell-centered Lagrangian scheme for multi-material compressible flows. Part II: the two-dimensional case, *J. Comput. Phys.* 312 (2016) 416–442.
- [59] J.R. Kamm, F.X. Timmes, On Efficient Generation of Numerically Robust Sedov Solutions, Technical Report LA-UR-07-2849, Los Alamos National Laboratory, 2007.